Thermal and Electrical Conductivity Probe (TECP) for Phoenix

Aaron P. Zent,[1] Michael H. Hecht,[2] Doug R. Cobos,[3] Gaylon S. Campbell,[3] Colin S. Campbell,[3] Greg Cardell,[2] Marc C. Foote,[2] Stephen E. Wood,[4] and Manish Mehta[5]

Received 29 November 2007; revised 1 August 2008; accepted 30 November 2008; published 25 March 2009.

[1] The Thermal and Electrical Conductivity Probe (TECP) is a component of the Microscopy, Electrochemistry and Conductivity Analyzer (MECA) payload on the Phoenix Lander. TECP will measure the temperature, thermal conductivity, and volumetric heat capacity of the regolith. It will also detect and quantify the population of mobile H_2O molecules in the regolith, if any, throughout the polar summer, by measuring the electrical conductivity of the regolith as well as the dielectric permittivity. In the vapor phase, TECP is capable of measuring the atmospheric H_2O vapor abundance as well as augmenting the wind velocity measurements from the meteorology instrumentation. TECP is mounted near the end of the 2.3 m Robotic Arm and can be placed either in the regolith material or held aloft in the atmosphere. This paper describes the development and calibration of the TECP. In addition, substantial characterization of the instrument has been conducted to identify behavioral characteristics that might affect landed surface operations. The greatest potential issue identified in characterization tests is the extraordinary sensitivity of the TECP to placement. Small gaps alter the contact between the TECP and regolith, complicating data interpretation. Testing with the Phoenix Robotic Arm identified mitigation techniques that will be implemented during flight. A flight model of the instrument was also field tested in the Antarctic Dry Valleys during the 2007–2008 International Polar Year.

Citation: Zent, A. P., M. H. Hecht, D. R. Cobos, G. S. Campbell, C. S. Campbell, G. Cardell, M. C. Foote, S. E. Wood, and M. Mehta (2009), Thermal and Electrical Conductivity Probe (TECP) for Phoenix, *J. Geophys. Res.*, *114*, E00A27, doi:10.1029/2007JE003052.

1. Introduction

[2] Phoenix will be the first Martian lander to operate at polar latitudes, affording a unique opportunity to study the current climate, the role of surface-atmosphere exchange, and the polar climate record in the structure and distribution of ground ice. It will make the first measurements to constrain volatile and energy fluxes in a region that is key to Martian climatic evolution and the first physical and chemical analyses of Martian ground ice. By combining observations of present-day processes, and the geologic record of past processes, Phoenix will provide fundamental insights into Martian history, and its astrobiological potential [*Smith et al.*, 2008].

[3] The Thermal and Electrical Conductivity Probe (TECP), a component of the Microscopy, Electrochemistry and Conductivity Analyzer (MECA) on the Phoenix Lander, will address these topics. On the basis of the small, dual-probe sensors that are routinely used to monitor soil thermal properties and water content, TECP performs six distinct measurements: dielectric permittivity, electrical conductivity, temperature, thermal conductivity, volumetric heat capacity, and relative humidity. In addition, application of the thermal properties protocol when the TECP is held aloft by the Robotic Arm (RA) allows constraints to be placed on the average wind speed.

[4] This paper describes the TECP, its measurements, its design and implementation, its calibration, characterization and field testing, as well as some of the anticipated science results. The importance of the TECP data set is enhanced by the uniqueness of the Phoenix landing site in the Martian polar regions.

1.1. High Martian Latitudes

[5] The Phoenix Lander touched down on 25 May 2008 at 68.16°N, 233.35°E, (Figure 1) [*Arvidson et al.*, 2008], an area that is fairly typical of the Vastitas Borealis plains. Investigation of a near-polar landing site gives us the opportunity to characterize a part of Mars that is more dynamic, and arguably, over the past several 10^7 years at least, more globally significant, than previous landing sites. Many components of the Martian climate are effectively controlled, or play out most dramatically, at these latitudes.

1.1.1. H_2O Reservoir

[6] The high-latitude surface is underlain by probably the largest H_2O reservoir on the planet. Substantial permafrost

[1]Planetary Systems Branch, NASA Ames Research Center, Moffett Field, California, USA.
[2]Jet Propulsion Laboratory, Pasadena, California, USA.
[3]Decagon Devices, Pullman, Washington, USA.
[4]University of Washington, Seattle, Washington, USA.
[5]Department of Atmospheric, Oceanic and Space Sciences, University of Michigan, Ann Arbor, Michigan, USA.

0148-0227/09/2007JE003052

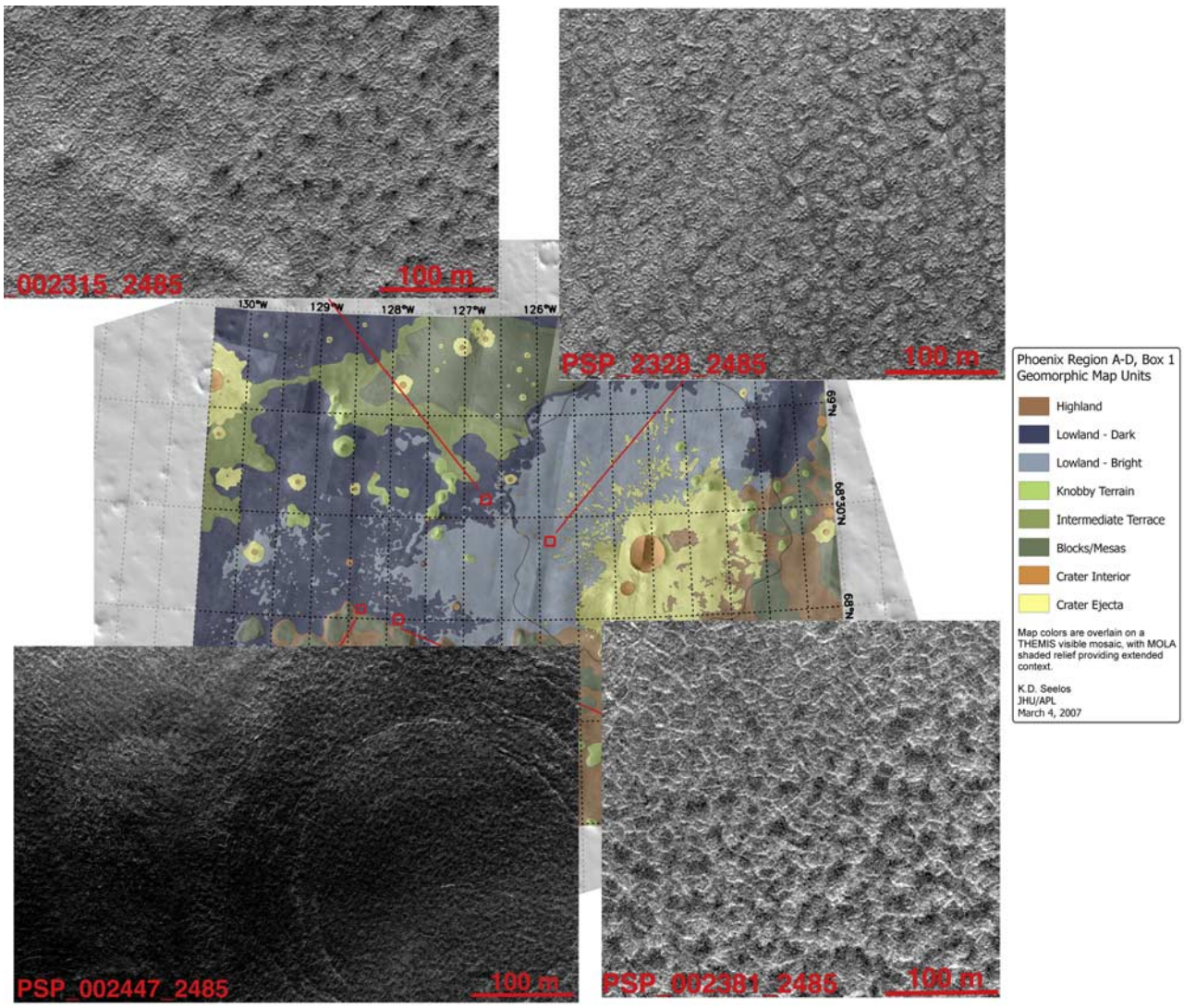

Figure 1. Geologic map of the Phoenix landing site by K. D. Seelos [see *Arvidson et al.*, 2008], with examples of patterned ground seen in High Resolution Imaging Science Experiment imagery (all examples ~50 cm pixel^{-1}).

deposits were first predicted on energy balance considerations [*Leighton and Murray*, 1966]. Post-Viking, there was supporting geomorphic evidence for wide spread ground ice at high latitudes [*Rossbacher and Judson*, 1981; *Squyres*, 1986]. The presence of high-latitude ice deposits were confirmed by Mars Odyssey [*Boynton et al.*, 2002].

[7] Among the criteria for choosing the Phoenix site was that the modeled Odyssey GRS data suggest that the dry overburden thins somewhat at these longitudes; access to both the ground ice and its dry overburden were considered fundamental objectives.

1.1.2. Seasonal Cycle

[8] The Phoenix landing site is also part of the circumpolar terrain covered annually by the seasonal CO_2 cap. Within the seasonal cap perimeter, the surface energy balance controls the condensation of H_2O and CO_2. Cap condensation and sublimation are the dominant climatic processes in the current epoch. Phoenix is well placed to observe and begin characterization of cap condensation processes.

[9] Once the seasonal cap has retreated poleward of the Phoenix site, the high-latitude regolith is likely a source of H_2O to the atmosphere, which along with cap, buffers planetary atmospheric H_2O [*Jakosky*, 1983]. Depending on the thermal and diffusive properties of the regolith, H_2O vapor exchange with the ground ice could have a major impact on the annual atmospheric water budget [*Schorghofer and Aharonson*, 2005]. Results from the Planetary Fourier Spectrometer (PFS) suggest the possibility that atmospheric H_2O is preferentially concentrated in the lowest few kilometers of the surface at high northern latitudes during summer [*Tschimmel et al.*, 2008]. If true, this would affect the upper boundary condition in atmospheric H_2O, and hence subsurface ice stability models.

1.1.3. Obliquity Effects

[10] In addition to the important role the polar regolith plays in determining seasonal cycles, the high latitudes experience the most extreme variations over orbital oscillations. In particular, variations in orbital obliquity have a pronounced effect on polar temperatures. At low obliquity,

variations in polar insolation over the year are minimized. It was formerly believed that semipermanent CO_2 caps would form at both poles at minimum obliquity [*Toon et al.*, 1980; *Pollack and Toon*, 1982; *Fanale et al.*, 1982], cold trapping regolith ice away. More recent modeling however, calls into question the nature of the cap at low obliquity [*Haberle et al.*, 2003; *Armstrong et al.*, 2004].

[11] When obliquities are high, the polar regions experience extreme seasonal insolation variations. The north polar H_2O cap becomes unstable at some obliquity between 35° and 45° [*Mischna et al.*, 2003]. The stable location for ice at obliquities >45° is the low-latitude highlands, as first suggested by *Jakosky and Carr* [1985], but more recently supported by *Head et al.* [2003]. Because it is at the poles that obliquity variations have the most pronounced effect, the subsurface at the Phoenix site may provide a record of the processes and mechanisms that drive long-term climate change.

1.1.4. Periglacial Processes

[12] There are other similarities between the Martian high-latitude surface, and some of Earth's periglacial terrain. Understanding their true origin and nature is essential if we are to read the geologic record, both at the surface, and in the subsurface.

1.1.5. Polygonal Ground

[13] Much of the Northern Plains, including the Phoenix landing site, are covered with patterned ground that is remarkably similar in appearance to examples that are commonly seen at terrestrial polar latitudes (Figure 1) [*Arvidson et al.*, 2008; *McEwen et al.*, 2007]. Polygon formation begins with formation of a network of vertically propagating cracks due to the thermal contraction of ground ice during autumn and winter. *Mellon* [1997] modeled the process for the Martian climate and found the yield strength of frozen ground is exceeded during autumnal cooling, leading to mechanical failure and crack formation [*Lachenbruch*, 1962; *French*, 1996]. The cracks then accumulate either clastic particles, or, if it is available, liquid water. It is also possible to condense additional H_2O vapor in these cracks, a process that could likewise contribute to the accumulation of excess ground ice [*Fisher*, 2005].

[14] At current pressures and temperatures, liquid water is not stable on Mars long enough to fill the cracks, but past conditions may have permitted this process [*Costard et al.*, 2002]. Whether these features are relict of freeze-thaw cycles, due solely to thermal contraction, or are the product of other processes is a key question that Phoenix must resolve.

1.1.6. Excess Ground Ice

[15] The Gamma Ray Spectrometer on Mars Odyssey shows the presence of an ice-rich layer with unexplained abundances of more than 60% of ice by volume [*Boynton et al.*, 2002; *Feldman et al.*, 2002]. Buried H_2O deposits, such as snow, layered with dust [*Mischna et al.*, 2003] are a possible explanation for the large amount of interstitial ice, but periglacial freeze-thaw cycles could produce the same result.

[16] During freezing events, as the freezing front penetrates downward into the surface, unfrozen, interfacial water is removed to the ice phase, creating a hydraulic gradient along which additional water migrates. As long as the total (sensible + latent) heat flux carried by unfrozen water from below can balance the diffusion of heat upward to the surface, the freezing front will remain stationary, and ice lenses will develop in freezing soil. Once the regolith beneath the freezing front is depleted of H_2O, the sensible + latent heat flux to the freezing front is no longer sufficient to balance conduction, and the freezing front again begins to propagate to depth. This continues until another wet zone is reached, and another ice lens begins to form. Terrestrial periglacial terrain often exhibits numerous ice lenses in the shallow subsurface.

1.1.7. Habitability

[17] The thermal physics of Martian permafrost are also of interest because Earth's high-latitude permafrost, which bears many morphological similarities to the Phoenix landing site, is a rich habitat for psychrophiles. *Rivkina et al.* [2000] argue, on the basis of growth metabolism in the laboratory, that if the temperature is stable, as in deep permafrost, the minimum temperature for growth is perhaps 253 K. Growth metabolism is easily detectable at 263 K [*Finegold*, 1996].

[18] *Price and Sowers* [2004] reviewed the literature on psychrophilic life, and could find no detectable lower temperature limit for metabolism. They concluded that the extremely low energy costs of survival energy enable microbial communities in extreme environments to survive indefinitely. They also reported evidence for survival-level metabolism all the way down to 233 K, meaning that much of the Martian regolith and ground ice qualifies as "survivable" if only thermal limits are considered.

[19] *Jakosky et al.* [2003] examined the minimum temperatures at which interfacial unfrozen water can exist, the minimum subfreezing temperatures at which terrestrial organisms can grow and multiply, and the maximum temperatures that can occur in Martian high-latitude and polar regions to see if there is overlap. They concluded that high-latitude Martian ground ice was just at the limit of being habitable.

[20] The most probable lifetime limitation is exposure to galactic cosmic rays [*Kminek et al.*, 2003]; an accumulation of damage eventually overwhelms the cell's repair mechanisms. *Kminek et al.* [2003] predicted that the time required to reduce a viable spore population to 10^{-6} would be $<6 \times 10^5$ years in the top meter of the regolith, and $<7 \times 10^4$ years in the otherwise favorable upper 10 cm.

[21] *Zent* [2008] used a time-resolved thermal model of the subsurface, tuned to the Phoenix landing site, along with the 10-Ma orbital calculations of *Laskar et al.* [2004], to calculate several possible 10 Ma thermal histories of Phoenix's target ice. In all cases, there were many clement periods when growth, even rapid growth, was possible. Also however, in every case, the maximum dormancy period that must be survived was at least an order of magnitude greater than the $\sim 7 \times 10^4$ years quoted by *Kminek et al.* [2003].

1.2. Science and Measurement Objectives

[22] The science objectives of the Phoenix mission are (1) to study the history of Martian water in all its phases and (2) to search for evidence of habitable zone and assess the biological potential of the ice-soil boundary.

[23] The polar regolith holds a substantial fraction of the remaining Martian H_2O inventory, and is a dynamic reser-

voir for H_2O over both seasonal and astronomically driven climate cycles. The abundance, distribution, and structure of polar ground ice may also have preserved a geologic record of the recent climate and subsurface conditions. Finally, as we have already discussed, polar ground ice may be just at the margin of habitability.

[24] The TECP was included on Phoenix specifically to determine the regolith thermophysical properties that control energy fluxes between the atmosphere and subsurface, to characterize the processes that control the distribution and exchange of H_2O between the atmosphere and subsurface in the current climate, and to document the occurrence of any unfrozen water, both as thin films in the regolith, and as atmospheric vapor.

1.2.1. Science Objectives

1.2.1.1. Energy Fluxes

[25] Regolith thermal properties, particularly the thermal conductivity (κ) and the volumetric heat capacity (C_V) are key, and currently unknown, parameters in any model that purports to address the distribution of Martian ground ice, the climatic cycles associated with variations in orbital parameters, or the annual cycles of H_2O and CO_2. These properties determine how effectively heat conducts from the illuminated surface to depth, and fix the thermal profile from the surface down at least as far as the ice table.

[26] On the basis of these measurements, estimates of the thermal inertia of the surface can be made, and compared with thermal inertias that are derived from measurement of the surface temperature throughout a thermal cycle, whether by TECP itself, or with thermal inertias derived from orbital data [e.g., *Mellon et al.*, 2000].

1.2.1.2. Regolith H_2O

[27] Another set of objectives involves understanding the abundance, state, and mobility of H_2O in the regolith. H_2O redistributes itself continuously through the regolith, continually accumulating in the lowest-energy reservoir that is thermodynamically available. Because soil and ice coexist in the regolith, it is necessarily true that there is a finite and variable population of unfrozen H_2O molecules; if sufficiently thick films of unfrozen water occur, surface diffusion in the film can outstrip diffusion in the vapor phase. These mobile H_2O molecules are most easily detected in measurements of soil electrical properties, which are otherwise dominated by highly insulating silicates and ice.

[28] Because TECP can measure both unfrozen water and temperature over a diurnal cycle, it may be possible to characterize both the soil water characteristic curve (the relationship between soil water content and soil water pressure potential) as well as the hysteresis curve of H_2O adsorption in the regolith materials. These are key parameters in determining the flow and transport of unfrozen water in the regolith.

1.2.1.3. Atmosphere

[29] The atmosphere serves as the conduit through which H_2O is distributed around the planet, and as the upper boundary condition controlling the state and distribution of H_2O throughout the regolith. Exchange between the atmosphere and regolith is controlled substantially by the absolute humidity of the atmosphere, and somewhat to a lesser extent by the wind fields. Therefore, TECP will also measure atmospheric relative humidity, and, by applying the same protocol used to determine regolith thermal properties, can constrain average wind speeds averaged over the duration of the measurement.

1.2.2. Measurement Objectives

[30] The following are the measurement objectives for TECP:

[31] 1. Measure the temperature of the Martian regolith, both at the surface, and within the excavation trench, as a function of Local Solar Time (LST), and the subsolar angle (L_s) which is used to express Martian seasons. If different types of materials can be accessed, these measurements will be repeated over the same time scales for each material. On the basis of surface temperature observations [*Kieffer and Titus*, 2001], measurement requirements on the temperature range from 165 K to 323 K, with 2 K precision and an accuracy of ±10%.

[32] 2. Measure the thermal conductivity and heat capacity of accessible Martian regolith materials. The TECP thermal conductivity requirement is to measure soil thermal conductivity (κ) with 10% accuracy over the range 0.03 – 2.5 W m^{-1} K^{-1}. A typical value for thermal conductivity in frozen soils or solid ice is $\kappa = 2.0 \pm 1.0$ W m^{-1} K^{-1} at $T =$ 223 K. This value is from many earth observations over many types of soil, including pure ice. We concluded that we would not require TECP to measure pathologically low thermal conductivity, since the landing event and the measurement attempt itself would probably destroy any such fluffy surface; simply confirming an off-scale low κ would be useful. Note that for such a surface the thermal inertia, $I = \sqrt{\kappa c \rho} = 0.03$ (W m^{-1} K^{-1}) 800 (J kg^{-1} K^{-1}) 1350 (kg m^{-3}) = 180, which is extremely low. The upper limit on the thermal conductivity requirement was a result of heritage design constraints. Thermal conductivities above 2.5 W m^{-1} K^{-1} result in very small temperature increases at the heated needle, which are difficult to resolve with the 12-bit ADC. The volumetric heat capacity (C_V) of a particulate mixture is the heat capacity of each component, weighted by its volumetric relative abundance; or approximately the specific heat of the regolith times its density. The requirement for the instrument is to measure the volumetric heat capacity of the regolith with 10% accuracy over range 0.4 to 4 MJ m^3 K^{-1}, which approximately spans the range from dry frozen ground to nearly the heat capacity of liquid H_2O (4.19 MJ m^3 K^{-1}) [*Hinkel et al.*, 2001; *Kane et al.*, 2001].

[33] 3. Measure the electrical conductivity (inverse of the electrical resistivity) of the regolith materials, particularly as a function of measured regolith temperature. The requirements for electrical conductivity are to measure soil and ice electrical conductivity from 10^7 nS cm^{-1} to 1 nS cm^{-1} with 10% accuracy. Conductivity, (σ) is a property of a material (e.g., copper), as opposed to conductance, which is a property of a specific conductor (e.g., a wire made of copper). Conductivity has units of Siemens per meter (S m^{-1}); we will typically use (nS cm^{-1}) (1 S m^{-1} = 10^7 nS cm^{-1}). Deionized water has a conductivity of 5.5×10^{-6} S m^{-1} (55 nS cm^{-1}); Siberian permafrost has been measured with electrical resistivity, R, as high as 1.4×10^4 Ω m ($\sigma =$ 715 nS cm^{-1}) at depth >2.2 m just before warming begins [*Olhoeft*, 1978; *Pozdnyakov and Chan*, 1979].

[34] 4. Measure the bulk dielectric permittivity of the regolith materials over the range of 1 to 20, with resolution of 0.005, as a function of regolith temperature. The dielectric permittivity of any gas is ~1, and ε for water is 78.54.

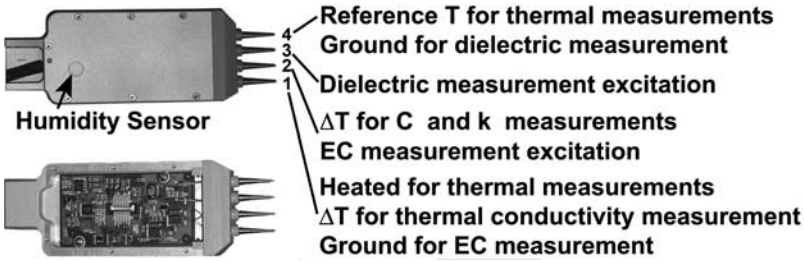

Figure 2. (top) Photograph of the Thermal and Electrical Conductivity Probe (TECP) instrument and (bottom) with the external cover removed to allow access to the electronics board. For each needle, the numerical designation and functionality is identified at right. The TECP is 118.76 mm in length. Its needles are 15 mm long.

We chose not to measure the full range because high sensitivity (hence high resolution) is desired at the low end of the range to maximize sensitivity to small changes in the abundance of unfrozen water. The upper limit of 20 is imposed because MECA data words are only 12 bits, so achieving sensitivity of 0.005 at the low end of the range limited the upper limit of the dynamic range to 20. The relationship between the water content of a soil and dielectric permittivity is complex and continues to be studied [*Topp et al.*, 1980; *Jones and Or*, 2003; *Lebron et al.*, 2004; *Sweeney et al.*, 2007]. The overall dielectric is the sum of the dielectrics of air, mineral, ice and water. In a nonfrozen system, we typically assume unfrozen water is the only constituent changing in the medium; all other dielectrics stay the same. The change in dielectric permittivity can then be interpreted solely in terms of the change in unfrozen water. However, T changes will affect permittivity as well; therefore all ε measurements are carried out with simultaneous T measurements of the medium.

[35] 5. Measure the H_2O vapor density of the Martian atmosphere as a function of LST, L_s, and height above the surface, including measurements made within the trench and particularly just above the ice layer if an ice layer is detected. TECP also includes a GE Panametrics MiniCap 2 polymer relative humidity (R_H) sensor, a commercial capacitive polymer-based sensor whose performance at temperatures and frost points below 233 K was not well known initially (see the Calibration Discussion, below). The requirement is to measure the H_2O vapor pressure from 0 – 0.5 kPa over the temperature range of 195 K – 270 K, with accuracy of ±10% of reading. Because the sensor is sensitive to R_H, the absolute partial pressure can only be determined with a measurement of air temperature. Strategies for determining absolute H_2O partial pressure are discussed below. An additional consequence of this approach is that the resolution in absolute pressure is a function of the sensor temperature, which is related to, but not identical to, the air temperature.

[36] 6. Measure, or characterize, the wind speed as a function of LST, L_s, and height, including within the trench.

2. Technical Approach

[37] In order to meet the measurement requirements, TECP was developed as a single electronics box, (Figure 2) integrated with four needle-like "probes," each of which has a role as a component in a unique set of circuits (Figure 3). The TECP needles are fitted into a plastic housing, which in turn is attached to the instrument electronics box. The plastic interface is machined from polyethylethylketone (PEEK), which has low thermal and electrical conductivity (κ = 0.249 W m^{-1} K^{-1}; C_V = 2.177 kJ kg^{-1} K^{-1}), and provides insulation between the thermally and electrically activated needles and the electronics box. The aluminum electronics housing is anodized to increase emissivity, enhancing thermal radiation, and minimizing heating when TECP is operating in direct sunlight. A port in the side of the instrument housing allows the relative humidity sensor to access the Martian atmosphere. The sensor is shielded behind a Teflon membrane that is porous to atmospheric H_2O but prevents dust from fouling the humidity sensor.

[38] TECP has a single rotational degree of freedom relative to the RA, (Figure 4), which in turn has 3 degrees of freedom relative to the lander and the environment.

2.1. Temperature

[39] The temperature of three of the needles (1, 2, and 4) is measured as the difference between the sense and reference junctions of a Type E (chromel-constantan) thermocouple. The thermocouple was fabricated by soldering the ends of a 7.5 cm piece of constantan thermocouple wire to the ends of two 7.5 cm pieces of chromel thermocouple with Kester Sn63Pb37 rosin core solder and Indium Flux 1. The reference junction of the thermocouple is on the TECP analog electronics board, adjacent to a National Semiconductor LM234DT temperature-sensing current source. The temperature derived from this element is referred to as the board temperature (T_b); the output current is directly proportional to the absolute temperature, and extrapolates to zero at 0 K.

2.2. Thermal Properties

[40] The in situ thermal properties of the Martian regolith are determined via the transient heated needle technique [*de Vries*, 1952]. In this approach, a heat pulse is applied via a heater that approximates a line source, and the thermal response of the medium is measured at some radial distance from the heat source.

[41] In addition to thermocouples, needles 1, 2, and 4 are also equipped with resistance heaters. The heater is Evanohm, an alloy used extensively for precision wound resistors. Its composition is nominally 0.75 Ni, 0.20 Cr, 0.025 Al, and 0.025 Cu. The Evanohm is dipped in lacquer because the thermal grease used to ensure good thermal

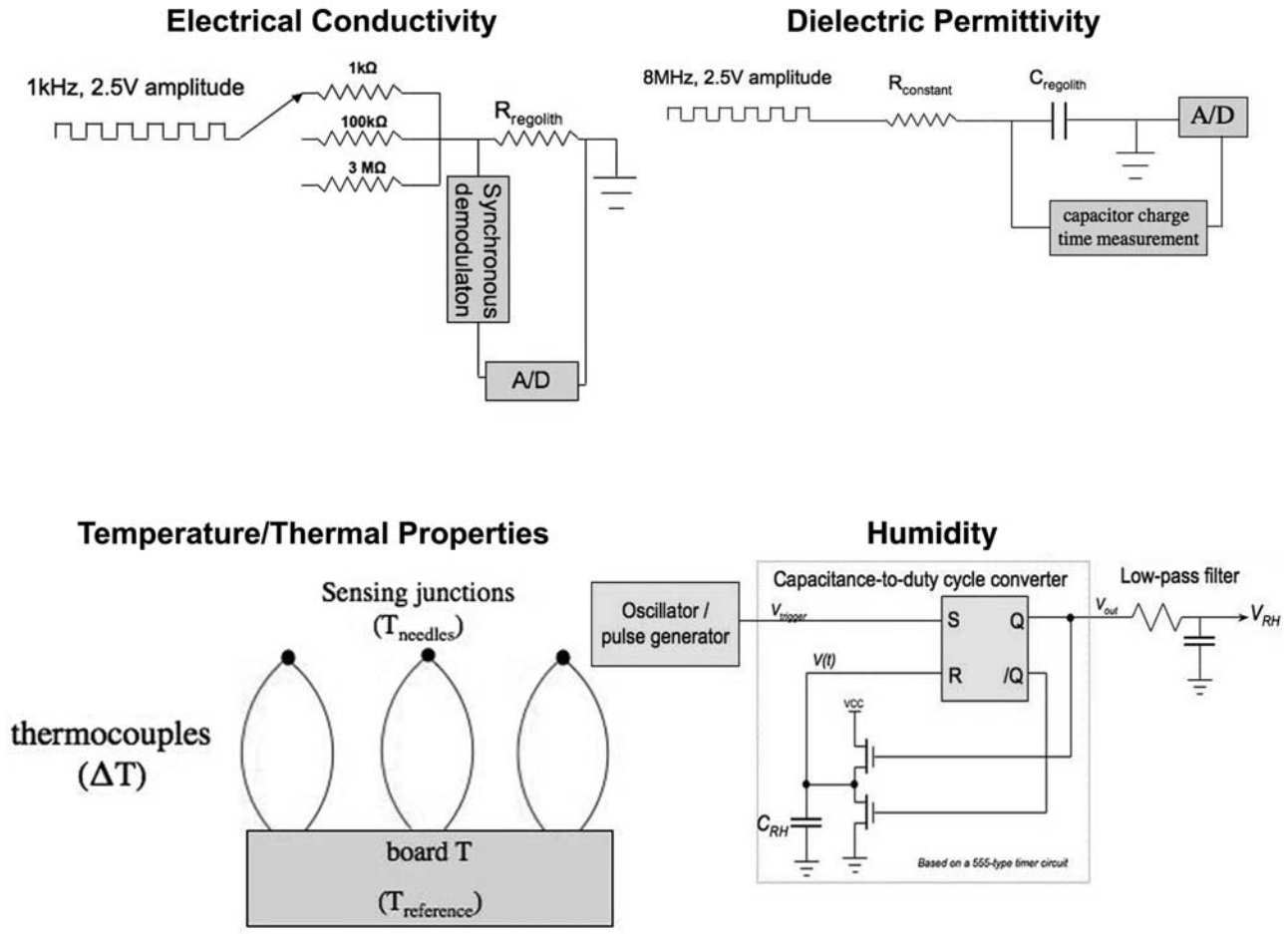

Figure 3. The electrical circuits employed by TECP to measure electrical and thermal properties of the regolith and atmosphere.

contact to the needles has a metallic component, which would cause the heater to short to the needles.

[42] In typical operations, needle 1 is heated and the temperature change of both needle 1 and needle 2 is monitored. The temperature change of needle *i,* between time 0 and time *t* is determined from

$$\Delta T_{i,t} = \left(T_{i,t} - T_{4,t}\right) - \left(T_{i,0} + T_{4,0}\right) \quad (1)$$

Needle four (farthest from the heated needle) is used as a temperature reference, as it is unaffected by the heat pulse from the needle for heat pulses of normal duration. This method also has the advantage of removing the effects of thermal drift of the bulk material or the TECP electronics board during the measurement.

[43] *Carslaw and Jaeger* [1959] modeled the temperature surrounding an infinite line heat source with constant heat output and zero mass, in an infinite medium. When a constant amount of heat is emitted from unit length of a zero-mass heater over a period of time, the temperature response at radial distance *r*, is

$$\Delta T_{t,i} = -\frac{q}{4\pi\kappa} Ei\left(\frac{-r^2 C_V}{4\kappa t}\right) 0 < t < t_1 \quad (2)$$

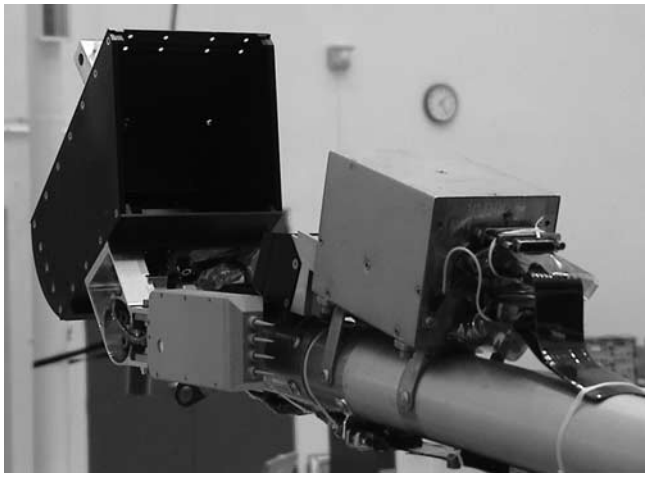

Figure 4. The TECP mounted on the Robotic Arm (RA). The Robotic Arm Camera (RAC) is at right and can image either the scoop contents or the TECP when it is rotated counterclockwise for use.

where q is the rate of heat dissipation (W m^{-1}), t_1 is the heating time, and Ei is the exponential integral. The temperature change after the heat is turned off is given by

$$\Delta T_{t,i} = -\frac{q}{4\pi\ \kappa}\left[-Ei\left(\frac{-r^2 C_V}{4\kappa\ t}\right) + Ei\left(\frac{-r^2 C_V}{4\kappa(t-t_1)}\right)\right] t > t_1 \quad (3)$$

Material thermal properties are determined by fitting the time series temperature data during heating to equation (2) and during cooling to equation (3); note that the absolute temperature T doesn't enter into the calculation, only ΔT. Thermal conductivity and heat capacity can be obtained from the temperature of the heated needle (single needle), with r taken as the radius of the needle and independently by fitting equations (2) and (3) to the temperatures measured at the adjacent needle, 7 mm from the heated needle.

[44] For the fitting procedure, a multistage Monte Carlo method described by *Conley* [1985] is used to obtain values close to the global minimum, and then a Marquardt method is used to find the final values. The exponential integral function was approximated using formulae from *Abramowitz and Stegun* [1972].

[45] The outputs of the solver function are κ_{f1} and C_{f1}, which are the thermal conductivity and volumetric heat capacity measured at the heated needle (needle 1), and κ_{f2} and C_{f2}, which are thermal conductivity and volumetric heat capacity measured at the adjacent needle (needle 2). The values for κ_{fi} and C_{fi} found via fitting to equations (2) and (3) are inherently inaccurate owing to inevitable discrepancies between the TECP and the mathematically idealized model. However, the true thermal properties can be determined if functional calibration is performed against materials of known thermal properties as described below.

2.3. Dielectric

[46] To measure the dielectric permittivity of the regolith, two of the needles (3 and 4) are used as the plates of a capacitor; with the regolith serving as the dielectric. The measurement involves putting a microwave frequency (~6.25 MHz) voltage square wave on the capacitor, and measuring the time history of the charge on the plates.

[47] The time, t, required to charge a capacitor from an initial voltage (V_i) to a final voltage (V_f), with an applied voltage (V) is

$$t = -RC\ln\left(\frac{V_f - V}{V_i - V}\right) \quad (4)$$

where R is the series resistance and C is the capacitance. The capacitance, in turn, is a function of the dielectric permittivity of the medium between the plates (or in this case, the regolith between the needles)

$$C = \varepsilon L_C \quad (5)$$

where L_C is a geometric factor that encompasses the area of the capacitive plates and their separation. L_C has units of length (m). The relationship between the time history of the plate charge and the dielectric permittivity is then

$$\frac{1}{\varepsilon} = \frac{1}{t}\left[-RL_C\ln\left(\frac{V_f - V}{V_i - V}\right)\right] \quad (6)$$

Because we are measuring the effective permittivity of a mixture of phases, rather than a pure phase, we refer to the measured quantity as the bulk dielectric permittivity (ε_b).

2.4. Electrical Conductivity

[48] The electrical conductivity (σ) of the soil is measured between needles 1 and 2. The regolith conductance (G_R), the inverse of the regolith resistance (R_R), is measured via a simple voltage divider (Figure 3). Three fixed resistors (R_F = 1 kΩ; 100 kΩ; 3 MΩ) are used to allow the 12-bit data word to cover the entire dynamic range specified in the requirements with sufficient precision. This results in three distinct measurement channels, each with its own effective range, which are measured sequentially.

[49] The input voltage (V_i) is 2.5 V, and the resistance of the regolith is found from the output voltage (V_o) via

$$R_R = \frac{V_o}{V_i}\left(\frac{R_F}{\left(\frac{V_i}{V_o} - 1\right)}\right) \quad (7)$$

The conductivity of the regolith is found by multiplying conductance ($1/R_R$) by the probe constant (C_P), which in effect normalizes for the geometry of the electric field that permeates the regolith between the needles. The determination of the probe constant is described below.

2.5. H_2O Vapor

[50] The TECP H_2O measurement is based on a GE Panametrics MiniCap 2 polymer relative humidity sensor. It is a capacitance-based instrument that measures the permittivity of a polymer film which adsorbs H_2O. The circuit in the TECP is read out in a manner similar to the capacitance measurement already described for the soil measurement.

[51] Solid state humidity sensors of this type are sensitive to relative humidity, almost independent of temperature. Specifically, the R_H is measured relative to the equilibrium pressure of liquid H_2O, rather than ice, regardless of temperature. At $T < 273$ K, the saturation vapor pressure of supercooled water is used.

[52] The physical basis for this behavior is likely that atmospheric H_2O forms an adsorbed film on the sensing polymer in equilibrium with the atmosphere, and it is the thickness of this adsorbate that is actually sensed as a change in permittivity It can be shown that, for many adsorbents, the mass (or thickness) of this adsorbed layer is nearly the same for a given R_H, regardless of temperature [*Anderson*, 1995]. Above some limiting film thickness, corresponding to R_H = 100%, the thickness of the film increases without limit, and bulk H_2O condenses.

[53] Unfortunately, there is a low-temperature limit in humidity measurements of this type. To substantially affect the bulk permittivity of the sensing film, the H_2O molecules must be free to align with the applied electric field; that is they must remain "unfrozen." Should some of the water adsorbed in the sensing film undergo spontaneous crystallization to ice, the device would instantly lose sensitivity to that portion of H_2O, resulting in a discontinuity in sensor output.

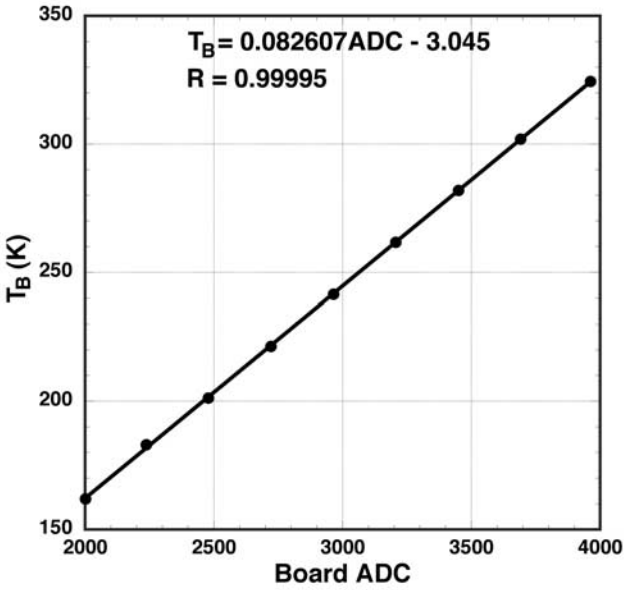

Figure 5. TECP Flight Model (FM) board temperature sensor calibration.

[54] One may think of the interfacial, unfrozen water in the sensor as being in dynamic equilibrium with the competing forces of the H_2O hydrogen bonds in ice, and the van der Walls bonds of adsorbing polymer. As T decreases below 273 K, the hydrogen bonds between H_2O molecules increasingly overcome the sum of the H_2O kinetic energy + the energy of the H_2O-polymer bond, and the maximum possible thickness of the unfrozen water layer decreases. At whatever temperature this ever-decreasing maximum reaches the film thickness corresponding to R_H = 100%, ice will condense, and the instrument will begin to lose sensitivity, beginning at the highest humidity. Experience suggests that in the TECP, this lower limit is reached ~205 K. Additional characterization work, and examination of the flight data will determine this limit more precisely.

[55] In TECP, the humidity sensor is located adjacent to the board temperature sensor on the analog electronics board, and T_b is used as a measure of the R_H sensor. Owing to power dissipation on the electronics board, T_b is typically slightly higher than the ambient air temperature during operation. This works to our advantage, in that it maintains the sensor above the frost point when the atmospheric R_H is high. However, it also means the R_H of the sensor is lower than that of the atmosphere. In practice, however, we can use the measured R_H along with T_b to calculate the absolute humidity of the atmosphere. If an estimate of atmospheric R_H is desired, it can be calculated from absolute humidity along with an independent atmospheric temperature measurement, such as those made by the meteorology payload.

3. Calibration

3.1. Temperature

3.1.1. Board Temperature Sensor

[56] The board temperature sensors were calibrated to NIST traceable temperature standards in a two part process. Opening the flight units and attaching temperature sensors directly to the boards was not an acceptable option, so an Engineering Model (EM) unit was used to characterize the temperature difference between T_b and the temperature at the outside of the TECP enclosure (on the aluminum cover directly above the board temperature sensor). NIST traceable temperature references were then attached to the flight TECP units above the board temperature sensors and measured while the TECP was brought to temperatures over its full expected temperature range. The correction determined on the EM unit was then applied and the board temperature calibration function was determined.

[57] The temperature difference between the PCB and the analog board cover varied smoothly as a function of temperature according to

$$\Delta T = -4.3917 \times 10^{-6} T^2 + 2.8044 \times 10^{-4} T + 0.64736 \quad (8)$$

with R^2 = 0.996. This polynomial was applied to the calibration data.

[58] Diode type, NIST traceable temperature sensors (Lake Shore Cryotronics model DI-470) were attached with Kapton tape to the TECP aluminum cover directly over the board temperature sensors on the TECP flight units. The TECP units were placed in an aluminum thermal enclosure in a Delta Design environmental test chamber. The chamber was used to bring the thermal enclosure and TECP to equilibrium at eight temperatures: 160 K, 180 K, 200 K, 220 K, 240 K, 260 K, 280 K, and 323 K. During post-processing, the difference between T_b and the analog cover temperature (equation 8) was applied to the temperatures measured by the diode sensors. Figure 5 shows the calibration function for T_b on the TECP flight unit.

3.1.2. Thermocouple Calibration

[59] Thermocouple calibration involved determining the Seebeck Coefficient (C_S) versus temperature for the thermocouple alloys used in the TECP needles. This allows accurate determination of the temperature difference between the TECP needles and T_b. The Seebeck Coefficient measured here was from the same spool used to fabricate the flight model thermocouples.

[60] Two cylindrical pieces of copper 1.3 cm long × 4.6 cm diameter were bolted 6.5 cm apart on a piece of acrylic, which was set on top of a block of open cell foam in a Delta Design temperature chamber. The two blocks each had a 3.2 mm diameter hole bored to their center from the rounded surface which housed precalibrated temperature sensors and thermocouple junctions. The thermocouple junctions and NIST traceable temperature sensors were colocated and potted in the borehole in the copper blocks with Arctic Silver high thermal conductivity grease.

[61] In one of the blocks, a 0.4 cm hole was bored completely through the block to facilitate a 180 Ω electrical heating element, allowing the block temperature to be controlled independently, and thus achieve a temperature difference between the two thermocouple junctions (Figure 6).

[62] The Delta Design temperature chamber was used to control the temperature of the atmosphere around the thermocouples. Seebeck coefficients were determined for the thermocouple at approximately 30 K increments from 150 to 330 K. The blocks were allowed to equilibrate at each ambient temperature setting for at least 30 min. At

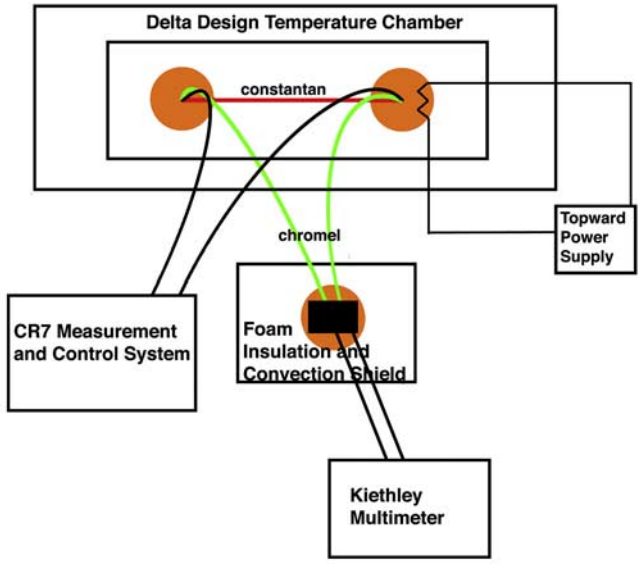

Figure 6. The calibration setup for the thermocouple calibration.

each ambient temperature, a voltage between 0 and 32 V was applied to the heater in the copper block producing a temperature difference (ΔT) between the two blocks. At least 60 s were allowed to pass between the final voltage adjustment and the recording of data to ensure that the system was in thermal equilibrium.

[63] Figure 7 shows the Seebeck coefficient versus temperature data collected here, which closely follow a third-order polynomial function. The Seebeck coefficient function shown here is used to calculate the temperature difference between the needles and T_b on the flight unit.

3.2. Thermal Properties

[64] The TECP thermal properties measurement functions were calibrated at the system level. Measurements in materials of known thermal properties were used to construct a calibration function for the thermal conductivity measurement and volumetric heat capacity measurement for TECP in a manner described by *Cobos et al.* [2006] and summarized here.

[65] TECP thermal properties time series data sets were collected in five materials with known thermal properties (Table 1). The Macor ceramic, high-density polyethylene (HDPE), and glycerol were obtained from commercial vendors. The expanded polystyrene (EPS) was obtained from a larger block of certified material used as a thermal conductivity calibration standard at Decagon Devices. The water was stabilized with agar powder at a mixing ratio of 5 g l^{-1} to prevent convective heat loss from the heated needle.

[66] In the case of the stabilized water and glycerol, thermal properties values were taken from published reference literature. The thermal properties of the Macor and HDPE samples were determined with a commercial thermal properties meter (model KD2 Pro, Decagon Devices), which was calibrated immediately prior to testing. The EPS material is a commercially available, NIST traceable thermal conductivity standard material obtained from LaserComp, Inc. The volumetric specific heat of the foam standard was calculated calorimetrically from published values of the specific heat and density of polystyrene and the measured density of the EPS.

[67] All measurements were taken in a dry box using a vertical stage to insert the TECP needles into the standard materials. An N_2 purge was used during measurement of the glycerol, which is hygroscopic. The stabilized water and glycerol were contained in 600 ml beakers, into which the TECP was lowered until the metal sensing needles were fully immersed in the fluid, but the PEEK shoulders were not. The TECP sensing needles were inserted into the EPS block using the vertical stage, and were again inserted until the needles were fully encased, and the PEEK shoulders were not. The HDPE and Macor samples were machined to accommodate the four TECP needles. A total of six needle holes were machined into the HDPE and Macor blocks, with the center two holes purposely cut slightly undersized to ensure that the cones of needles 1 and 2 made solid thermal contact with the material. This resulted in a small gap between the PEEK shoulder and the calibration block. Before inserting the TECP into the Macor and HDPE blocks, all of the holes were completely filled with DI water to promote thermal contact between the needles and the material. The excess water that was forced from the holes during the insertion of the TECP was removed from the surface of the material block with a pipette. After insertion into each material, the system was allowed to come into thermal equilibrium before data were collected. Additionally, between repeated measurements on the same sample, the system was also allowed to come back to thermal equilibrium after introduction of the preceding heat pulse.

[68] For each thermal properties measurement, the TECP control software was configured to record the output of the board temperature sensor, the three needle thermocouples, and the heater current sense resistor at 1 Hz for 160 s. A 60 s

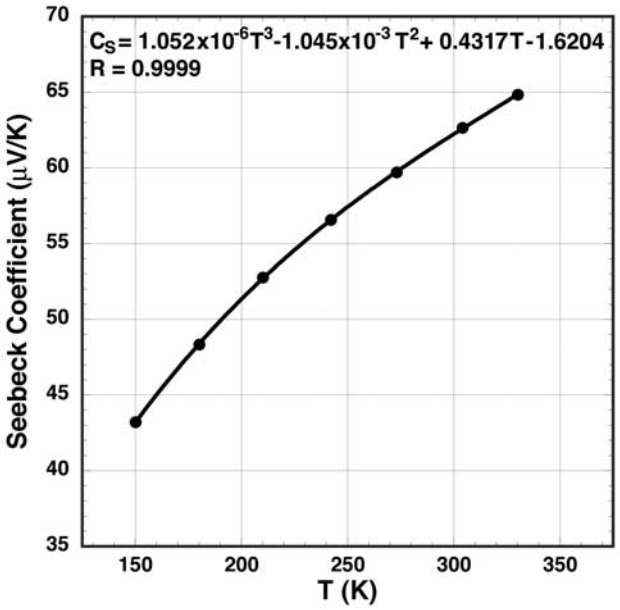

Figure 7. The Seebeck Coefficient of the thermocouple wire used for the TECP FM.

Table 1. Thermal Properties Standard Materials Used in the TECP Calibration[a]

Material	Thermal Conductivity (W m^{-1} K^{-1})	Thermal Conductivity Source	Heat Capacity (kJ m^{-3} K^{-1})	Heat Capacity Source
Macor (glass ceramic, 25°C)	1.402	Decagon	2010	Decagon
Water (stabilized, 25°C)	0.608	CRC	4174	CRC
HDPE (23°C)	0.513	Decagon	1690	Decagon
Glycerol (20°C)	0.285	*Ganiæ and Hicks* [1991]	2963	*Ganiæ and Hicks* [1991]
Expanded polystyrene (EPS, 20°C)	0.033	Laser Comp	63	Calculation

[a]TECP, Thermal and Electrical Conductivity Probe.

heat period was applied to needle 1 after an initial 10 s buffer period with no heat. After cessation of the heat pulse, 90 s of cooling data were recorded. Each thermal properties measurement was repeated at least twice in each material. For the glycerol, the needles were removed and reinserted into the same sample between measurements. For the stabilized water, the needles were removed from the first sample and inserted into an identical, virgin sample between measurements. For the EPS, the needles were removed and inserted into a virgin section of the same block of the material. For the HDPE sample, the needles were removed from the sample, and the orientation of the sample was reversed so that needle 1 was in the hole formerly occupied by needle two. For the Macor sample, two measurements were made in the original orientation, and two in the reversed orientation for a total of four measurements.

[69] The measured thermal conductivity (κ_m) and heat capacity (C_m) are related to the values derived from the fitting process by the following calibration functions:

$$\kappa_m = C_1\kappa_{f1} + C_2\kappa_{f2} + C_3C_{f1} + C_4C_{f2} + C_5 \quad (9)$$

$$C_m = C_6\kappa_{f1} + C_7\kappa_{f2} + C_8C_{f1} + C_9C_{f2} + C_{10} \quad (10)$$

The calibration coefficients $C_1 \ldots C_{10}$ were determined during calibration by minimizing the error between actual values (κ_a and C_a), and the measured values (κ_m and C_m) determined in equations (9) and (10). Values for κ_{f1}, κ_{f2}, C_{f1}, and C_{f2}, generated from the MSMCO-Marquardt fitting process for the five materials tested are shown in Table 2. The relationship between the measured values, derived from equations (9) and (10), and the actual values for the five known calibration materials results in the relations shown in Figures 8 and 9, which are the final conversion from the measured to actual κ and C_V values.

3.3. Dielectric

[70] TECP dielectric measurements were taken in a series of four fluids with relative dielectric permittivities from 1 to 20 (Table 3). Each of the fluids was housed in a 30.4 cm diameter by 17.5 cm depth glass bowl, filled to within 1 cm of the top. Earlier finite element analysis and experimental testing showed that >95% of the electromagnetic field generated by the TECP dielectric measurement was contained within this volume for all calibration fluids. All measurements were performed in a dry box under dry N_2 purge; the TECP was lowered into the fluids with a translation stage. The TECP units were inserted into the fluid until the needles were submerged. For the air, isopropyl, and 1-decanol samples, the fluids were allowed to equilibrate to the temperature of the dry box for at least 1 h prior to data collection. The tert-butanol sample was held at a steady, above-ambient temperature with an electrical heating pad owing to its high melting temperature (301 K). In each fluid, data were collected from the TECP unit for 25 min to assure thermal equilibrium between the needles and the fluid. Thermal drift was not identified in any of the samples after one minute of equilibration time, so the TECP output values presented are the averages of approximately the final 24 min of data collection.

[71] Prior to making TECP measurements in the fluids, six subsamples of each of the three measured alcohols were collected. The fluids were transferred to 100 ml, septae-equipped, airtight glass containers in the dry box under N_2 purge. The relative dielectric permittivity of the standards was independently determined at the National Institute of Standards and Technology's Dielectric and Magnetic Mate-

Table 2. Thermal Conductivity (κ) and Heat Capacity (C_V) Values Measured at Needle 1 and 2 With the TECP Flight Unit[a]

Material	κ_{f1}	κ_{f2}	C_{f1}	C_{f2}	κ_m	$C_{V,m}$	κ_a	$C_{V,a}$
EPS	0.110	0.199	1.741	1.539	0.033	0.065	0.033	0.063
EPS 2	0.112	0.202	1.727	1.545	0.034	0.061	0.033	0.063
Glycerol	0.498	0.526	1.815	5.149	0.283	2.913	0.285	2.96
Glycerol 2	0.517	0.534	1.669	5.097	0.291	2.823	0.285	2.96
Water	0.936	1.071	1.077	7.232	0.595	4.296	0.606	4.17
Water 2	0.951	1.125	1.086	7.348	0.614	4.367	0.606	4.17
Water 3	0.942	1.035	1.131	6.728	0.602	4.097	0.606	4.17
Macor	1.629	2.846	0.409	3.095	1.391	2.008	1.401	2.02
Macor 2	1.636	2.832	0.401	3.149	1.392	2.059	1.401	2.02
Macor 3	1.682	2.947	0.351	3.085	1.441	2.024	1.401	2.02
Macor 4	1.634	2.904	0.377	3.151	1.404	1.986	1.401	2.02
HDPE	0.683	1.062	1.268	3.484	0.501	1.679	0.513	1.691
HDPE2	0.694	1.122	1.199	3.627	0.514	1.693	0.513	1.691

[a]The values of κ_m and $C_{V,m}$ are generated from equations (12) and (13), and the known values of κ_a and $C_{V,a}$ are taken from literature or other sources.

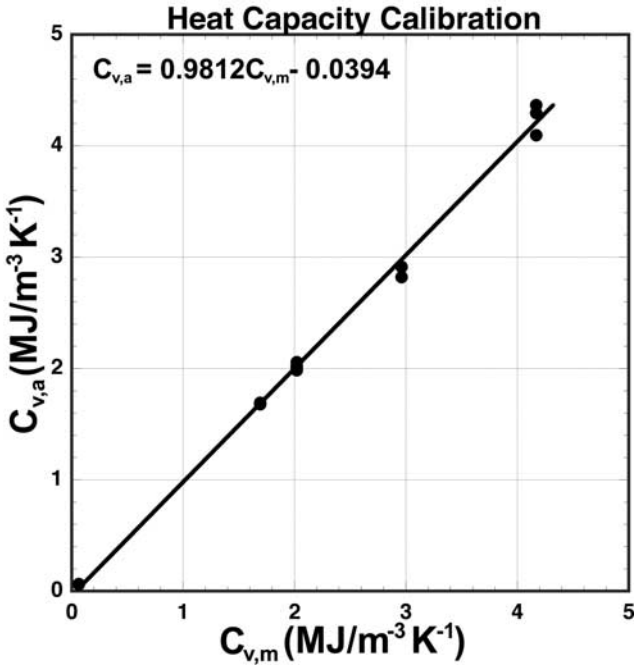

Figure 8. The volumetric heat capacity calibration curve. $C_{v,a}$ is the volumetric heat capacity of the laboratory standard materials, and $C_{v,m}$ is the measured heat capacity, which is actually derived not through direct measurement, but through fitting equations (9)–(10) to the measured heating and cooling curves associated with heating one of the needles.

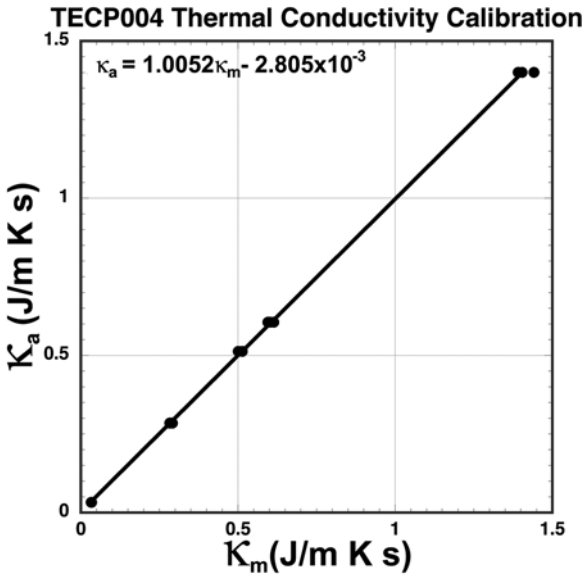

Figure 9. The thermal conductivity calibration curve. The thermal conductivity of the laboratory standard materials is κ_a, and κ_m is the measured thermal conductivity, which is actually derived not through direct measurement, but through fitting equations (9)–(10) to the measured heating and cooling curves associated with heating one of the needles.

rial Laboratory. The NIST measurements were performed with two different parallel plate devices at the same measurement frequency (6.25 MHz) and temperature as the TECP calibrations. Using the data in Table 3, the TECP calibration function was determined (Figure 10).

3.4. Electrical Conductivity

[72] The electrical conductivity calibration was a two-step process. First, the TECP conductivity function was characterized with a set of fixed resistors. Second, aqueous standard solutions were used to find the probe constant versus resistance. By combining these two functions, the electrical conductivity of the bulk medium surrounding the needles can be accurately determined for each of the three resistance channels (Table 4).

[73] The TECP flight unit was placed in the Delta Design chamber. Copper blocks machined at the same cone angle as the TECP needles were used to make electrical contact between the needles and two clip-type leads that were routed through mouseholes to the exterior of the chamber. The resistance of the leads was measured at 0.06 Ω, and has been neglected in the following analysis. The clip leads were used to sequentially connect the TECP needles across a series of 24 axial lead resistors ranging from 50 Ω to 250 MΩ. The resistance of each of the fixed resistors was measured just prior to each TECP measurement with a calibrated Agilent multimeter. To allow circuit settling, data were collected across each resistor for 120 s for each of the three measurement ranges. The average of the last 10 s of TECP output for each measurement range has been used in all subsequent analyses. This process was repeated at five different temperatures, spanning the range 160 K to 323 K.

[74] Measurements were then taken in a series of six aqueous standard solutions ranging from 1 to 10,000 μS cm^{-1}. The standards were poured to 500 ml in a 600 ml Pyrex beaker. All experiments were performed in the dry box with the TECP lowered into the solutions with the translation stage until the metal needles were fully submerged. The PEEK shoulders were not submerged in the solution. Measurements began with the 1 μS cm^{-1} sample (DDI water), and progressed to the highest salt concentration sample. The TECP needles were wiped dry and wiped with an isopropyl alcohol clean room wipe between samples. Before measuring with the TECP, the conductivity of each solution was measured with a calibrated Orion multi meter. In the special case of the 1 μS cm^{-1} solution, where a very small amount of salt contamination would affect the conductivity of the standard significantly,

Table 3. Materials and Results Used in the TECP Dielectric Calibration[a]

Material	Nominal Dielectric	Temperature (°C)	NIST Dielectric	Output TECP Flight Model (ADC)
Air	1	23	1	642
1-decanol	7.5	24	8.07	1410
Tert butanol	10.9	32	11.22	2300
Isopropyl	18.3	23	19.76	4016

[a]NIST, National Institute of Standards and Technology; ADC, analog digital converter.

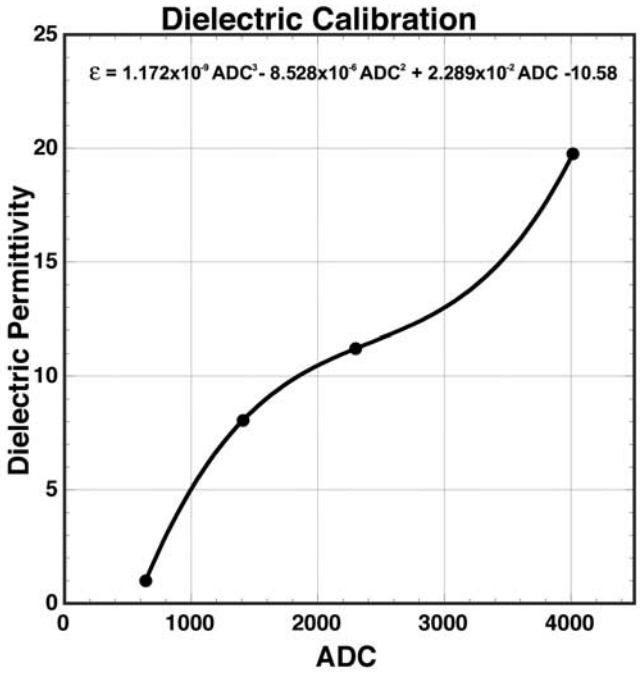

Figure 10. The dielectric permittivity calibration curve for the TECP flight unit.

the TECP was first dipped into the sample and removed, then the conductivity was measured with the Orion meter, and then the TECP was placed back into the sample and a measurement was taken. The calibration again consisted of a 120 s measurement in each of the three measurement channels. Again, the average of the last 10 s of TECP output for each measurement range has been used in all subsequent analyses.

[75] The data collected across the 24 resistors were used to construct a matrix of ADC output as a function of resistance and temperature for each channel. After each data set was abbreviated to its useful range (Table 4) it was modeled as a fourth-order polynomial function of TECP output versus ln resistance (Table 5).

[76] Preliminary characterizations indicated that the TECP probe constant (C_P) varies as a function of the measured resistance at least for the highest conductivity channel. The known resistance versus output functions determined above were used in conjunction with the measurements in standard solutions to determine the probe constant versus resistance relationship The probe constant is calculated by

$$C_P = \frac{10^6}{R\sigma} \tag{11}$$

where C_P is the probe constant (cm), R is the measured resistance (Ω), and σ is the electrical conductivity of the sample (μS cm^{-1}). The probe constant versus resistance functions is shown in Figure 11. Only the lowest conductivity solution (DDI water) fell within the useful resistance range of the low σ channel, so a cell constant versus measured resistance relationship could not be determined for the low σ function. The single point cell constant has been applied to all low σ function data described here.

3.5. H_2O Vapor

[77] Calibration of the TECP flight units for humidity was done at the University of Washington Mars Atmospheric Simulation Chamber (MASC) facility in March 2006. Over 50,000 humidity measurements at 5 to 30 s intervals were collected over a period of a week. The measurements covered a wide range of frost point temperatures (193 K – 263 K) and instrument temperatures (T_b 208 K to 303 K). Most of the data were collected under 500 Pa of CO_2 (7 mb), flowing through the chamber at ~200 cm^3 min^{-1} (STP). The absolute humidity was measured by two different NIST traceable chilled mirror hygrometers (an EdgeTech Dew-Prime I and a Buck Research CR-1).

[78] The air temperature in the chamber was typically a few degrees colder than T_b owing to self heating of the circuit board. This temperature difference, combined with the small anisothermality of the environmental chamber, prevented us from reaching higher relative humidities owing to ice formation in the chamber. For example, the vapor pressure corresponding to R_H = 0.60 at −55°C is equal to the saturation vapor pressure at −58.9°C.

[79] The ADC counts are related to T_b and the relative humidity, R_H, via a quadratic equation

$$ADC = -1.5332R_H^2 + (963.34 + 14.705T_b)R_H + \left(2804.7 - 1.0373T_b - 6.9089 \times 10^{-3}T_b^2\right) \tag{12}$$

This relationship was obtained by a least squares fit of nearly 12,000 data points using a six-parameter quadratic function of relative humidity and temperature, and has a standard deviation of 4.5 ADC counts (Figure 12). Applying the calibration involves plugging the board temperature into equation (12), and solving for the root of the quadratic.

[80] The sensor output voltage is measured with a 12-bit ADC, and has a minimum value (at R_H = 0) of around 2800 digital number (DN), and an apparently temperature-dependent maximum (at R_H = 100%) of at least 3200 DN (the highest value we observed). At 213 K the maximum value of the response function is only 2900, so this standard deviation represents a 5% error. However, at 233 K the increased range of response reduces the standard deviation to about 2%.

4. Laboratory and Field Characterization

[81] Although the TECP meets the measurement requirements as verified in the lab, practicalities of field and

Table 4. Useful Resistance Ranges for Each TECP Measurement Range

Channel	Minimum Resistance	Maximum Resistance
High conductivity (ECH)	–	6 kΩ
Medium conductivity (ECM)	6 kΩ	1 MΩ
Low conductivity (ECL)	156 kΩ	–

Table 5. The Coefficients for the Fourth-Order Polynomial Fit of ln(R) to the ADC Counts as a Function of Temperature

T (K)	High Range
160	$\ln(R) = -8.341 \times 10^{-14}\ \mathrm{ADC}^4 + 8.237 \times 10^{-10}\ \mathrm{ADC}^3 - 2.751 \times 10^{-06}\ \mathrm{ADC}^2 + 4.743 \times 10^{-03}\ \mathrm{ADC} + 3.136$
200	$\ln(R) = -7.892 \times 10^{-14}\ \mathrm{ADC}^4 + 7.927 \times 10^{-10}\ \mathrm{ADC}^3 - 2.691 \times 10^{-06}\ \mathrm{ADC}^2 + 4.718 \times 10^{-03}\ \mathrm{ADC} + 3.128$
240	$\ln(R) = -7.809 \times 10^{-14}\ \mathrm{ADC}^4 + 7.858 \times 10^{-10}\ \mathrm{ADC}^3 - 2.673 \times 10^{-06}\ \mathrm{ADC}^2 + 4.699 \times 10^{-03}\ \mathrm{ADC} + 3.136$
280	$\ln(R) = -7.742 \times 10^{-14}\ \mathrm{ADC}^4 + 7.807 \times 10^{-10}\ \mathrm{ADC}^3 - 2.661 \times 10^{-06}\ \mathrm{ADC}^2 + 4.690 \times 10^{-03}\ \mathrm{ADC} + 3.139$
323	$\ln(R) = -7.769 \times 10^{-14}\ \mathrm{ADC}^4 + 7.820 \times 10^{-10}\ \mathrm{ADC}^3 - 2.662 \times 10^{-06}\ \mathrm{ADC}^2 + 4.689 \times 10^{-03}\ \mathrm{ADC} + 3.141$
T (K)	Middle Range
160	$\ln(R) = -3.248 \times 10^{-14}\ \mathrm{ADC}^4 + 4.654 \times 10^{-10}\ \mathrm{ADC}^3 - 1.922 \times 10^{-06}\ \mathrm{ADC}^2 + 4.037 \times 10^{-03}\ \mathrm{ADC} + 7.918$
200	$\ln(R) = -3.248 \times 10^{-14}\ \mathrm{ADC}^4 + 4.654 \times 10^{-10}\ \mathrm{ADC}^3 - 1.922 \times 10^{-06}\ \mathrm{ADC}^2 + 4.037 \times 10^{-03}\ \mathrm{ADC} + 7.918$
240	$\ln(R) = -3.263 \times 10^{-14}\ \mathrm{ADC}^4 + 4.605 \times 10^{-10}\ \mathrm{ADC}^3 - 1.903 \times 10^{-06}\ \mathrm{ADC}^2 + 4.019 \times 10^{-03}\ \mathrm{ADC} + 7.905$
280	$\ln(R) = -3.128 \times 10^{-14}\ \mathrm{ADC}^4 + 4.498 \times 10^{-10}\ \mathrm{ADC}^3 - 1.877 \times 10^{-06}\ \mathrm{ADC}^2 + 4.000 \times 10^{-03}\ \mathrm{ADC} + 7.901$
323	$\ln(R) = -3.100 \times 10^{-14}\ \mathrm{ADC}^4 + 4.478 \times 10^{-10}\ \mathrm{ADC}^3 - 1.873 \times 10^{-06}\ \mathrm{ADC}^2 + 3.998 \times 10^{-03}\ \mathrm{ADC} + 7.901$
T (K)	Low Range
200	$\ln(R) = 1.3236 \times 10^{8}\ \mathrm{ADC}^3 - 1.1648 \times 10^{-4}\ \mathrm{ADC}^2 + 3.4326 \times 10^{-1}\ \mathrm{ADC} + 323.41$
240	$\ln(R) = 1.2165 \times 10^{8}\ \mathrm{ADC}^3 - 1.0593 \times 10^{-4}\ \mathrm{ADC}^2 + 3.0932 \times 10^{-1}\ \mathrm{ADC} + 286.57$
280	$\ln(R) = 1.9291 \times 10^{8}\ \mathrm{ADC}^3 - 1.7078 \times 10^{-4}\ \mathrm{ADC}^2 + 5.0553 \times 10^{-1}\ \mathrm{ADC} + 483.93$

spacecraft operation will affect the accuracy of the various measurements on the Martian surface. This section outlines some of those factors, and presents preliminary characterization data from the laboratory, spacecraft testbed activities, and field testing in the Antarctic Dry Valleys. Additional characterization work is underway to further improve science return from TECP.

4.1. Characterization

4.1.1. Needle Temperature Versus Regolith Temperature

[82] TECP can accurately measure the temperature of its individual needles. However, needle temperature may not be identical to the regolith or air temperature. If, for example, the thermal conductivity of the regolith is extremely low, the TECP needles may be equally coupled to the regolith and the TECP body.

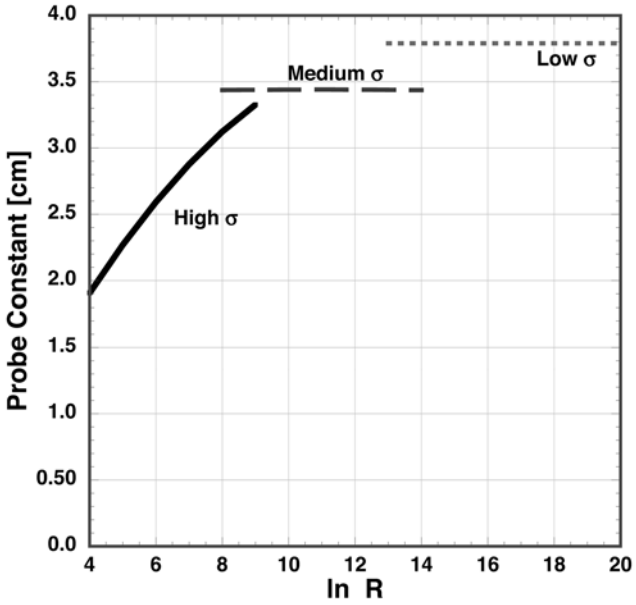

Figure 11. The probe constant for the TECP as a function of the resistance for each of the three channels of the electrical conductivity function.

[83] To characterize this effect, an experiment was conducted using three different test materials: water stabilized with agar, dry silt loam soil, and EPS. In each instance, the material was placed in a thermal chamber and brought to a

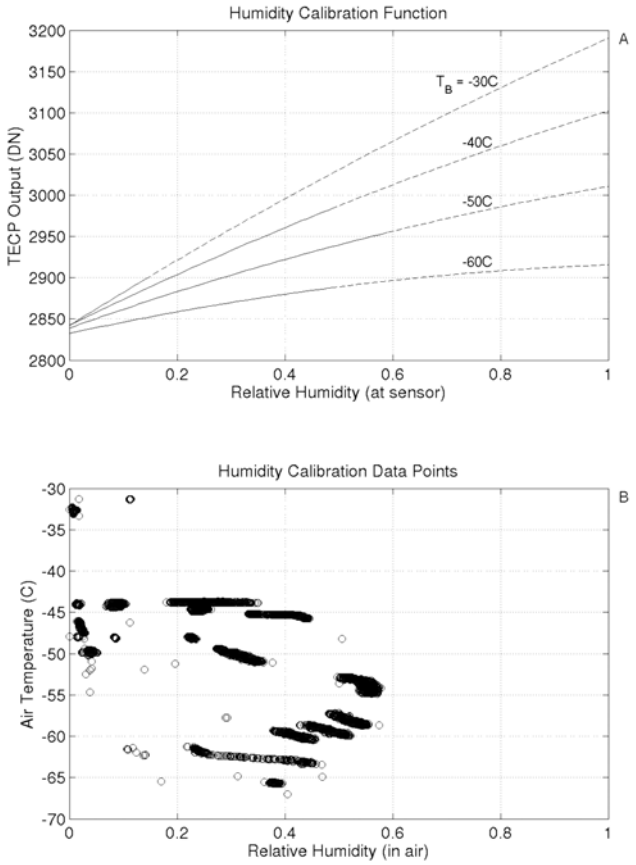

Figure 12. (a) Contours of the calibration function for the TECP humidity sensor at four different values of T_b. The dashed portions of each line indicate an extrapolation beyond the range of data used to derive the calibration function. (b) Scatterplot of the environmental conditions corresponding to each calibration data point.

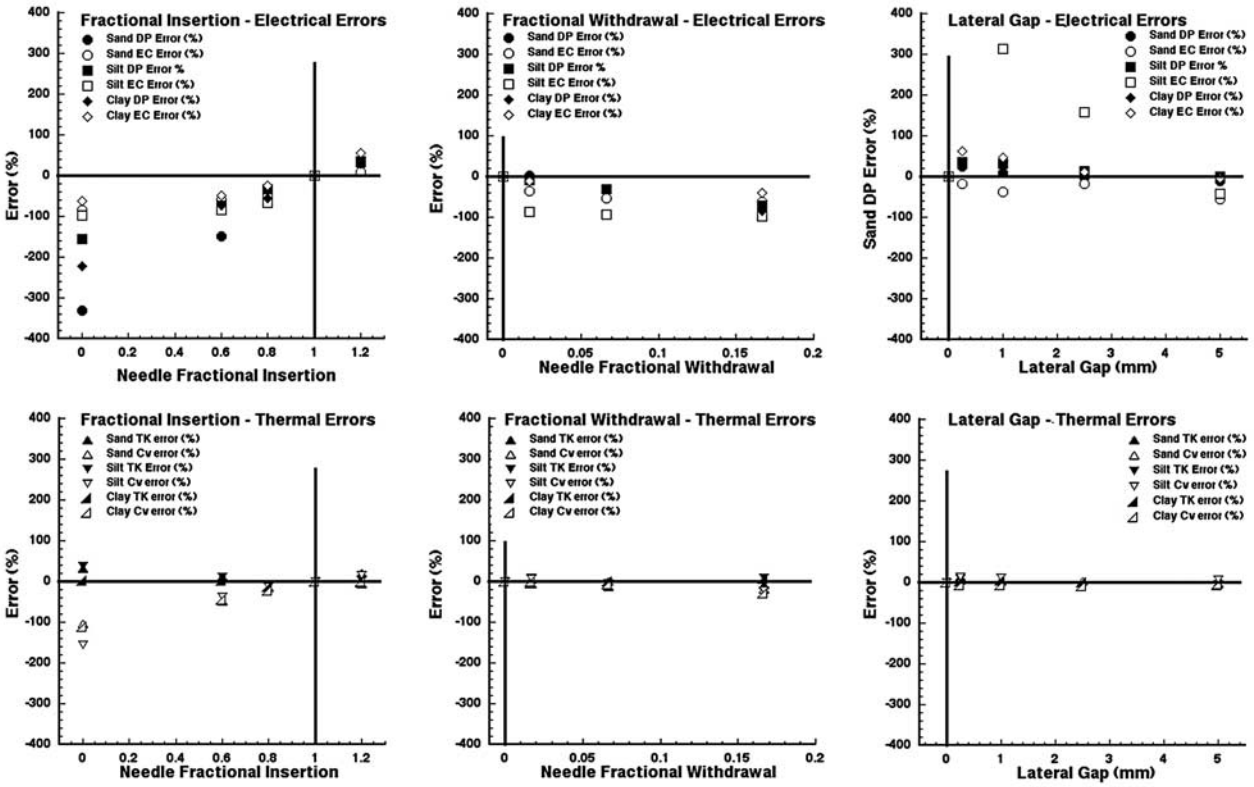

Figure 13. Errors introduced by incomplete and excess insertion, partial withdrawal, and lateral gaps in percent error deviation from an ideal insertion (marked with crosshairs).

temperature below ambient. The sample was then removed from the temperature chamber, placed in an insulating container at ambient pressure, and the TECP needles were inserted into the sample. The needle temperature, T_b, and sample temperature were monitored until they equilibrated, and then recorded. This process was repeated at different sample temperatures ranging from well below to well above the TECP temperature.

[84] It is apparent from the data that the error is linearly related to the temperature difference between the TECP body (T_b) and the needles: both measurable quantities. The slope of the linear relationship is, to first-order, linearly related to the thermal conductivity of the medium in which the TECP needles are inserted. Fortunately, thermal properties are based on ΔT measurements, and are independent of sample temperature. So, the preliminary characterization data presented here indicate that regolith temperature can be derived from measured needle temperature, T_b, and the independently measured regolith thermal conductivity.

4.1.2. Imperfect Needle Insertion

[85] In an idealized experiment, the TECP needles are fully seated in an infinite homogeneous half-space, with no voids either at the sides or at the end. However, in practice, the TECP will be put into use at the end of the 2.3 m Robotic Arm, and the possibility of gaps exists. Can measurements be made with imperfect placement?

[86] A series of experiments were conducted to understand the errors introduced into the various TECP measurements from (1) incomplete needle insertion; (2) complete insertion with partial retraction, and (3) complete insertion with lateral movement. The objectives were accomplished by using a manual mill to precisely control the position of TECP in relation to the sample, and create voids of known dimension. The materials tested during the incomplete insertion portion of this exercise were glycerol, stabilized water, AETB-8, a thermal protection foam, dry clay soil, dry silt loam soil, and dry quartz sand. All of these samples with the exception of the glycerol and stabilized water were tested in the partial retraction and lateral void exercises. The results of these experiments are summarized in Figure 13 for the three soils, and the salient points are described below. The description of mitigation approaches against nonideal insertions is deferred until the discussion of TECP Robotic Arm Interoperability tests (below).

4.1.2.1. Electrical Properties

[87] 1. One can think of the overdrive data as an investigation of the effects of compression on the sample, the partial retraction as the effects of air gaps, and the lateral movement experiment as their combined effects.

[88] 2. Progressive linear immersion of the needles in the soil particles has a more or less linear effect on measured permittivity, but an exponential effect on electrical conductivity.

[89] 3. Compaction increases the measured permittivity linearly, and the measured conductivity exponentially.

[90] 4. The creation of voids around the needles decreases the permittivity linearly, but decreases the measured conductivity exponentially.

[91] 5. In lateral motions, the effects of compaction initially dominate the electrical properties, but beyond 0.25 mm of lateral movement the effects of the voids appears to dominate.

[92] 6. The sensitivity of the measured electrical properties to the placement of the needle is proportional to their permittivity and conductivity. It is useful to look at the actual measured quantities, to see how the effects of insertion gaps are proportional to the permittivity and conductivity.

4.1.2.2. Thermal Properties

[93] 1. Although the heat capacity measurement is nicely behaved, varying linearly with insertion, and being relatively insensitive to compaction, the thermal conductivity results appear to be complicated by the data reduction technique.

[94] 2. Compression of the soil by the TECP results in linear increases in thermal properties, at least up to 3 mm, due to the loss of pore voids in the vicinity of the needles.

[95] 3. Voids result in linear decrease in the measured heat capacity, but the effects on the derived thermal conductivity are difficult to deconvolute from the idiosyncrasies of the mathematical modeling that must be done to extract κ.

[96] 4. In lateral motions, the effects of compaction initially dominate both the electrical and thermal properties, but beyond 0.25 mm of lateral movement, the effects of the growing voids become increasingly important.

4.1.3. Wind

[97] There are no requirements for TECP to measure wind velocity. However, application of a protocol similar to the thermal properties experiments has shown some promise in characterizing wind speeds, particularly in high-wind regimes where the wind sock associated with the Meteorology package is not capable of measuring wind as well.

[98] The procedure involves heating needle one for a period up to 70 s, and then following the cooling curve for another 90 s. Preliminary analysis of the heating and cooling data acquired at Mars-like pressures in a wind tunnel at the University of Michigan suggest that both peak temperatures and the cooling time constant

$$\tau_c = \frac{1}{T}\frac{\mathrm{d}T}{\mathrm{d}t} \tag{13}$$

are sensitive to wind velocity. Characterization of the TECP response to wind velocity is ongoing, and the determination of whether or not to try wind velocity measurements on the Martian surface will be made once those analyses are complete.

4.2. Antarctic Dry Valley Field Testing

[99] Field testing of a flight model unit, TECP010, was carried out in Beacon Valley, McMurdo Dry Valleys, Antarctica, during the 2007–2008 International Polar Year deployment.

4.2.1. Field Site and Data Collection

[100] The test site in Beacon Valley (77°50′24″S, 160°39′27″E) is at an elevation of 1400 m. The annual average temperature is −22°C. Snowmelt is confined to a layer $\leq$5 cm in depth on the basis of observations of oxidized soil horizons and salt concentrations. Below this, H_2O transport is restricted to thin films or vapor. At the time of the field observations, there was no snow cover, and the surface was visibly dry.

[101] The surface materials are silica-rich sands from the surrounding Beacon Sandstone, along with clastic fragments of dolerite, which occurs as intrusive sills throughout the Beacon Sandstone. The near surface is very rich in salts, predominantly mirabilite ($Na_2SO_4 \bullet 10H_2O$), halite, and a number of minor phases. Rocks and boulders are glacial erratics with a wide variety of compositions. Additional analyses of the sampled material are pending.

[102] During the austral summer, the sun does not set, so all measurements were conducted with the TECP, and the soil into which it was inserted, either in full sunlight, or shadow. Shadowing resulted from one of three sources. The TECP was placed near the north (afternoon sunlit) side of a pyramidal 30 × 19 × 17 cm rock. A Vaisala HM 34 Humidity and Temperature Sensor was placed next to it, and used periodically throughout data collection for comparison to the TECP humidity data.

[103] During the ''nighttime'' hours, (2100 h–0400 h), the sun illuminates the soil and face of the rock opposite the TECP (Figure 14, left). Between 0400 h and 0800 h, the entire site was shadowed by the steep valley walls. The sun emerged from behind the valley wall at ~0800 h, and for several hours, fully illuminated the TECP, the rock face, and the soil being sampled. Between 1700 and 1730 h, the shadow of the Science Tent, from which the TECP was operated, covered first the soil, then the TECP body itself, and finally the rock.

[104] Data collection spanned two periods, 2 January 2008 from ~2100 h to 0400 h, and the following day from 1540 h to 1940 h. Raw DN counts for each channel were converted to physical units via the functions published for TECP010 in the TECP Calibration Report. For the most part, the data set was nominal, and captured expected patterns in thermal and electrical properties. However, at least one anomalous and interesting event was recorded that merits explicit discussion.

4.2.2. Selected Results and Discussion

[105] Throughout the initial period of data acquisition, the TECP and soil were shadowed, although the rock and the soil opposite the TECP were continuously illuminated. Needle temperatures decreased steadily until ~0300 h. Beyond that, needle and board temperatures appear to be approximately stable, suggesting that the power dissipated by the TECP electronics is approximately balanced the heat loss of the TECP to the environment.

[106] The most interesting part of the data is the electrical properties. The Bulk Relative Permittivity (ε_b) decreases along with temperature until ~0215 h, and then begins a rapid increase (Figure 14, right). The total change from one time series to the next is greater than the variation within time series, suggesting that the effect is not due to noisy readings. The Electrical Conductivity data exhibit a somewhat different, but correlated response (not shown). Both the EC low and EC medium channels exhibit a sawtooth pattern; an abrupt drop in σ correlates with the minimum in the ε_b data, after which σ and ε_b increase sharply throughout the remainder of the night.

[107] This is a puzzling observation. At the temperature (265 K–270 K) and the frequencies of the TECP measure-

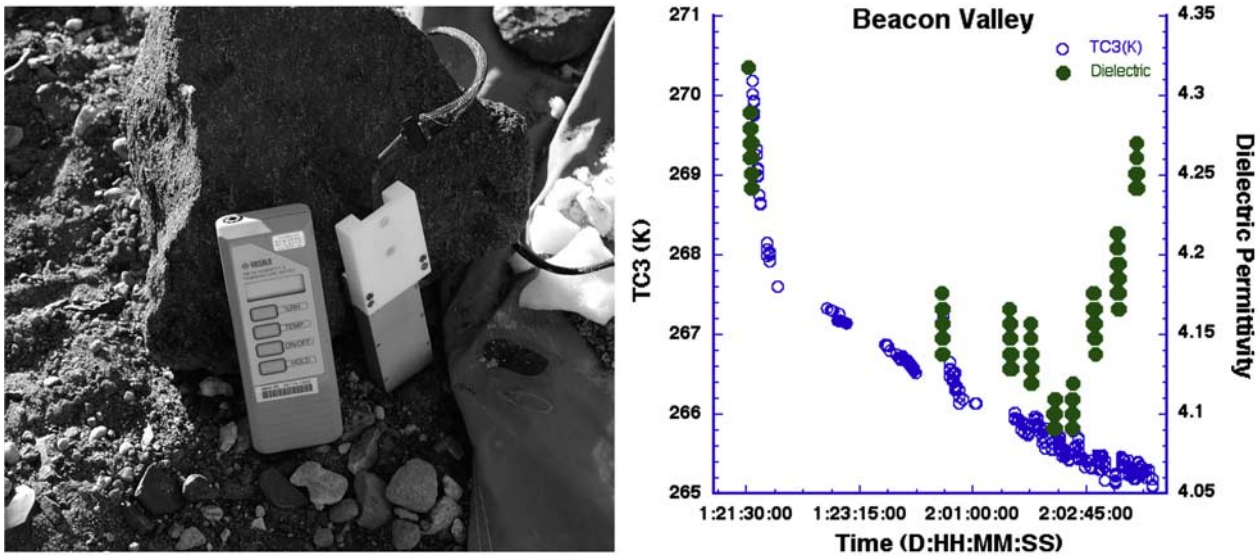

Figure 14. (left) The TECP deployed in Beacon Valley. (right) Needle 3 temperature and bulk dielectric permittivity recorded during the overnight hours of 2 January 2008.

ment (1 kHz for σ; 8 MHz for ε_b), both σ and ε_b are positively correlated with temperature in dry, rock-forming minerals [*Olhoeft*, 1981; *Buehler et al.*, 2005; *Napijalo et al.*, 1998]. The electrical properties change slope simultaneously, and approximately an hour before the cooling rate of the soil changed.

[108] Since the measurements were acquired in sublimation till above ice-cemented permafrost (depth to ground ice at the site was ~25 cm), and the R_H sensor registered a nonzero and stable atmospheric relative humidity in spite of ambient cooling, it is reasonable to suppose that there existed a population of unfrozen water on the surfaces of the soil particles. Normally, however, the volumetric unfrozen water content (θ) of soil in a closed system decreases as the temperature decreases, which would also be inconsistent with these observations.

[109] It is possible however, to increase ε_b and σ in a soil by adding unfrozen H_2O molecules, (open system). The correlation between the unfrozen water content and dielectric is a well-known phenomenon; there is even a "universal" relationship, which describes the relationship between ε_b and θ for a remarkably large variety of soil types [*Topp et al.*, 1980]

$$\varepsilon_b = 3.03 + 9.30\theta + 1460\theta^2 - 76.7\theta^3 \qquad (14)$$

Equation (14) assumes that a change in θ is the only variable affecting ε_b. If applied to the data recorded here, it would suggest an increase in unfrozen water of 0.25% between 0215 h and 0345 h (from 4.15% to 4.4%).

[110] The humidity data are stable, suggesting the atmosphere is not the source of H_2O molecules. An intriguing possibility, which may be consistent with the large $d^2\varepsilon_b/dt^2$ at 0215 h, is the arrival at the needles of additional H_2O molecules, migrating in thin films from the continuously warming far side of the rock. While this hypothesis requires further analysis, the unexpected relationships between thermal and electrical properties are suggestive of the type of events that might prove particularly exciting in data from the Martian surface.

4.3. Payload Interoperability Testbed Testing

[111] Since the measured electrical and thermal properties are so sensitive to the details of needle insertion, characterization of the interoperability of the Robotic Arm with the TECP were conducted in the Payload Interoperability Testbed (PIT) at the University of Arizona to assess the likely scope of gaps associated with nonideal insertion.

[112] The original goal was to conduct all TECP insertions along an angle of attack of <0.08 radians, which is the taper angle of the needles. However, this proved impracticable. Movement of the RA in the direction of the TECP needles (z axis) results in bouncing by several mm during start and stop transients, with the principle motions directed along the x and z axes (see Figure 15 for an example, and the coordinate axes referenced in the discussion). In the cohesive Baghouse Dust used in the PIT, this motion leaves needle tracks in the soil and affects the quality of the TECP insertion.

[113] To establish an operational baseline for the performance of the RA/TECP operations, we first conducted a manual insertion of the TECP into the Baghouse Dust, in a manner as near to ideal as possible. Results for various mitigation strategies were compared against the results of the ideal insertion to assess possible strategies for mitigating gap formation.

[114] The mitigating approach that proved most successful was to insert the TECP to the best of the RA capabilities, and then run the RASP for 15 s. The RASP is a small drill-like sampling device, included in the Robotic Arm Scoop in order to improve the chances of collecting very cold, and very hard, subsurface ice. In highly cohesive soils, the high-frequency, small-amplitude vibration caused by the RASP motor, coupled to the needles through the RA and TECP body, results in the collapse of any substantial voids surrounding the needles.

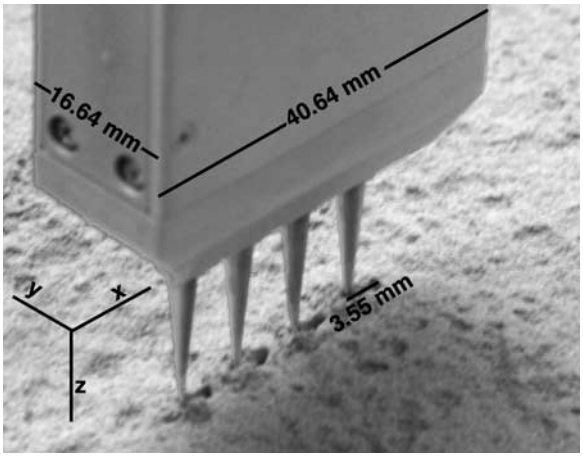

Figure 15. The TECP during interoperability testing with the Robotic Arm in the Payload Interoperability Testbed. The axes refer to the TECP-centered coordinate system used by the RA. The needle holes are evidence of overshooting in the *z* direction during a command move of + 1 cm in the *z* direction. Their shape reflects uncommanded movement of ~3.5 mm along the *x* axis.

[115] Of course, this technique does produce an alteration of the soil particulate structure from its original state, but the introduction of any measurement device will have the effect of disturbing the medium. Continued characterization efforts are underway to quantitatively assess the errors introduced by the nonideal insertions, combined with effects of the RASP to collapse the resulting voids.

4.4. Robotic Arm Camera Images

[116] One means of characterizing the cleanliness of any given insertion is by imaging the TECP with the Robotic Arm Camera (RAC). In Figure 16, the RAC has imaged the TECP during insertion tests, as a function of the rotation angle of the TECP relative to the RA. The insertion angles range from 30° to 77° (nearly orthogonal to the RA). In some instances, the entry point of at least one needle can be seen. As the rotational angle gets smaller, it is harder to verify insertion and possible gaps with the RAC. Other things being equal, we prefer to make measurements in an orientation that permits verification of TECP placement with the RAC. In any event, the RAC will image any area sampled by TECP both prior to insertion and immediately after retraction.

5. Surface Operations

[117] Operations Planning for TECP is somewhat unique for the Phoenix mission, because TECP is an in situ measurement of the regolith properties, which change with the environmental variables. In addition, by trenching in the regolith, we will alter the physical structure of the regolith, and disturb some of the properties we intend to measure. Because we do not yet know the rate at which trenching operations will occur, nor the total depth to ground ice, nor the physical configuration of the trench, nor the availability of undisturbed materials in the workspace accessible to the RA, actual scheduling and targeting decisions will have to be made as part of the strategic and tactical processes. However, some considerations are described below that should guide planning for TECP measurements during the expected mission.

[118] The physical and chemical activity of water is dependent upon temperature, and therefore, expected mission planning for characterization of regolith H_2O activity should focus on the local warmest period during operations.

[119] Landing occurred 25 May 2008 which corresponds to $L_s = 76°$, in the late northern spring. We can do the arithmetic very crudely and say there are 0.53842° L_s/Sol, so the approximate mapping of Mission Sol against L_s would indicate that summer solstice would occur around Sol 26 (Figure 17). This will be earlier than the local thermal maximum, and subsequent observations should be made approximately every 5° of L_s until after the local thermal maximum. Therefore, roughly, H_2O observation campaigns would also occur as follows:

$$L_s\ 95° = \text{Sol } 35$$

$$L_s\ 100° = \text{Sol } 44$$

$$L_s\ 105° = \text{Sol } 55$$

The ideal would be to do an insertion into the soil during the warmest part of the sol, and monitor the temperature, electrical conductivity, dielectric permittivity and R_H, but not thermal properties (heating during thermal properties measurements will alter, and perhaps redistribute H_2O) on or about sols 26, 35, 44, and 55.

[120] The desired insertion point, or points, cannot be determined in advance, because we do not know the

Figure 16. The RAC view of the TECP at insertion angles of (top) 30°, (middle) 47°, and (bottom) 77°.

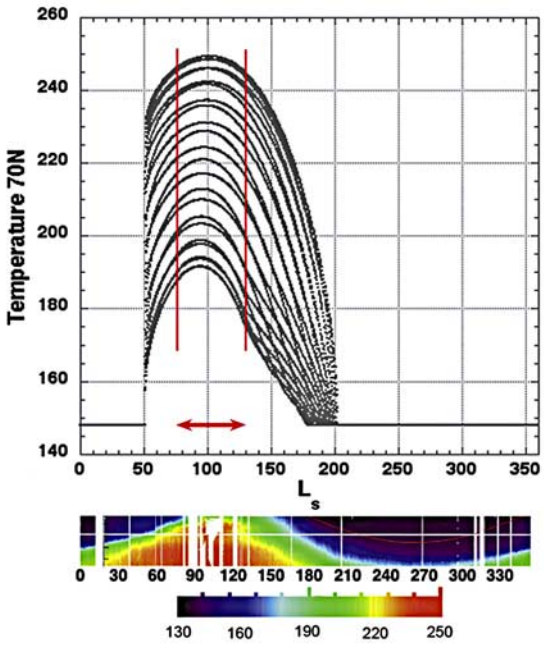

Figure 17. (top) The predicted surface temperature at 70°N. The arrow and vertical red lines indicate the nominal Phoenix mission duration. (bottom) Approximate surface kinetic temperature as measured by Thermal Emission Spectrometer on Mars Observer [*Kieffer and Titus*, 2001]. The horizontal white line indicates 70°N.

configuration of the trench at each date, the specific shadowing associated with the lander, the depth to the ice table and so on. However, the H_2O mobility campaigns should be conducted for an hour or two around the thermal maximum of a target selected during the tactical process in the sols leading up to the thermal campaign sols.

[121] The temperature and thermal properties should be measured in at least one material near the beginning ($L_s \sim 80°$), middle ($L_s \sim 105°$), and end ($L_s \sim 125°$) of the mission. These correspond roughly to sols 10, 50, and 90. The diurnal maximum surface temperature will change relatively little over the course of the mission, but the nighttime minima will vary considerably more (Figure 14). By targeting the beginning, middle, and end of the mission, we will be able to characterize the thermal properties of the accessible materials, as a function of temperature, over the greatest possible range.

[122] The temperature and thermal properties measurements should be conducted in material that is minimally disturbed. If horizontal compositional layering is evident in the dry overburden, each layer should be characterized.

[123] At least one of these thermal properties campaign days should be correlated with THEMIS observations of the Phoenix landing site, to characterize the relationship between in situ thermal properties measurements and those derived from remote sensing.

[124] Thus, a reasonable but modest regolith characterization campaign could be conducted by prioritizing TECP measurements on approximately 7 sols throughout the mission. The specific sols on which the H_2O and thermal properties are characterized can be decided tactically, but the rough guidelines given above will provide good coverage of temperature, and maximize the probability of catching any translational or rotational mobility in regolith H_2O molecules.

6. Summary

[125] The TECP will provide an exciting opportunity to measure the thermal properties of the Martian regolith in situ, as well as to characterize the response of the regolith in the high latitudes to the extreme variations in boundary conditions, both for temperature and H_2O abundance, that are characteristic of the polar summer. In combination with other Phoenix instruments, it is hoped that the physical and chemical processes associated with energy and H_2O fluxes through the regolith can be quantitatively understood in the present climate, and that this knowledge will give us the capability to decode the geologic history of the Martian polar latitudes as uncovered by the Phoenix mission.

[126] TECP is a thoroughly calibrated instrument, but there are practicalities of field and spacecraft measurements that must be taken into account. Mitigating procedures, such as using the Phoenix Robotic Arm RASP to collapse voids around the TECP needles are described. TECP was field tested in the Antarctic Dry Valleys, and showed promise in detecting small changes in unfrozen water under Antarctic conditions.

[127] **Acknowledgments.** The authors would like to thank John Michael Morookian, Troy Hudson, and Mike Janeczic, Roger Tanner, Tom Squire, Matt Switzer, Matt Siegler, Richard Quinn, Martin Buehler, Marsha Presley, Lynne Cooper, Nilton Renno, Bob Bonitz, Mike Shirbacheh, Matt Schneider, Adam Bruckner, and Carl Knowlen. Part of this research was carried out at the Jet Propulsion Laboratory, California Institute of Technology, under a contract with NASA.

References

Abramowitz, M., and I. A. Stegun (1972), *Handbook of Mathematical Functions*, Dover, London.

Anderson, P. S. (1995), Mechanism for the behavior of hydroactive materials used in humidity sensors, *J. Atmos. Oceanic Technol.*, *12*, 662–667, doi:10.1175/1520-0426(1995)012<0662:MFTBOH>2.0.CO;2.

Armstrong, J. C., C. B. Leovy, and T. Quinn (2004), A 1 Gyr climate model for Mars: New orbital statistics and the importance of seasonally resolved polar processes, *Icarus*, *171*, 255–271, doi:10.1016/j.icarus.2004.05.007.

Arvidson, R. E., et al. (2008), Mars Exploration Program 2007 Phoenix landing site selection and characteristics, *J. Geophys. Res.*, *113*, E00A03, doi:10.1029/2007JE003021.

Boynton, W. V., et al. (2002), Distribution of hydrogen in the near surface of Mars: Evidence for subsurface ice deposits, *Science*, *297*, 81–85, doi:10.1126/science.1073722.

Buehler, M. G., R. C. Anderson, and S. Seshadri (2005), Prospecting for in situ resources on the Moon and Mars using wheel-based sensors, *Proc. IEEE Aerosp. Conf.*, *2005*(1–4), 607–616.

Carslaw, H. S., and J. C. Jaeger (1959), *Conduction of Heat in Solids*, 2nd ed., Clarendon, Oxford, U. K.

Cobos, D. R., G. S. Campbell, and C. S. Campbell (2006), Modified line heat source for measurement of thermal properties on Mars, *Therm. Conduct.*, *28*, 331–338.

Conley, W. (1985), Linear systems revisited, *Simulation*, *45*, 15–18, doi:10.1177/003754978504500105.

Costard, F., F. Forget, N. Mangold, and J. P. Peulvast (2002), Formation of recent Martian debris flows by melting of near-surface ground ice at high obliquity, *Science*, *295*, 110–113, doi:10.1126/science.1066698.

de Vries, D. A. (1952), A nonstationary method for determining thermal conductivity of soil in situ, *Soil Sci.*, *73*, 83–90, doi:10.1097/00010694-195202000-00001.

Fanale, F. P., J. R. Salvail, W. B. Banerdt, and R. S. Saunders (1982), Mars: The regolith-atmosphere-cap system and climate change, *Icarus*, *50*, 381–407, doi:10.1016/0019-1035(82)90131-2.

Feldman, W. C., et al. (2002), Global distribution of neutrons from Mars: Results from Mars Odyssey, *Science*, *297*, 75–78, doi:10.1126/science.1073541.

Finegold, L. (1996), Molecular and biophysical aspects of adaptation of life to temperatures below the freezing point, *Adv. Space Res.*, *18*, 87–95, doi:10.1016/0273-1177(96)00003-8.

Fisher, D. A. (2005), A process to make massive ice in the Martian regolith using long-term diffusion and thermal cracking, *Icarus*, *179*, 387–397, doi:10.1016/j.icarus.2005.07.024.

French, H. M. (1996), *The Periglacial Environment*, 2nd ed., Longman, New York.

Ganiæ, E. N., and T. G. Hicks (1991), *The McGraw-Hill Handbook of Essential Engineering Information and Data*, McGraw-Hill, New York.

Haberle, R. M., J. R. Murphy, and J. Schaeffer (2003), Orbital change experiments with a Mars general circulation model, *Icarus*, *161*, 66–89, doi:10.1016/S0019-1035(02)00017-9.

Head, J. W., J. F. Mustard, M. A. Kreslavsky, R. E. Milliken, and D. R. Marchant (2003), Recent ice ages on Mars, *Nature*, *426*, 797–802, doi:10.1038/nature02114.

Hinkel, K. M., F. Paetzold, F. E. Nelson, and J. G. Bockheim (2001), Patterns of soil temperature and moisture in the active layer and upper permafrost at Barrow, Alaska: 1993–1999, *Global Planet. Change*, *29*, 293–309, doi:10.1016/S0921-8181(01)00096-0.

Jakosky, B. M. (1983), The role of seasonal reservoirs in the Mars water cycle II: Coupled models of the regolith, the polar caps, and atmospheric transport, *Icarus*, *55*, 19–39.

Jakosky, B. M., and M. H. Carr (1985), Possible precipitation of ice at low latitudes of Mars during periods of high obliquity, *Nature*, *315*, 559–561, doi:10.1038/315559a0.

Jakosky, B. M., K. H. Nealson, C. Bakermans, R. E. Ley, and M. T. Mellon (2003), Subfreezing activity of microorganisms and the potential habitability of Mars' polar regions, *Astrobiology*, *3*, 343–350, doi:10.1089/153110703769016433.

Jones, S. B., and D. Or (2003), Modeled effects on permittivity measurements of water content in high surface area porous media, *Physica B*, *338*, 284–290, doi:10.1016/j.physb.2003.08.008.

Kane, D. L., K. M. Hinkel, D. J. Goering, L. D. Hinzman, and S. I. Outcalt (2001), Non-conductive heat transfer associated with frozen soils, *Global Planet. Change*, *29*, 275–292, doi:10.1016/S0921-8181(01)00095-9.

Kieffer, H. H., and T. N. Titus (2001), TES mapping of Mars' north seasonal cap, *Icarus*, *154*, 162–180, doi:10.1006/icar.2001.6670.

Kminek, G., J. L. Bada, K. Poglianob, and J. F. Ward (2003), Radiation-dependent limit for the viability of bacterial spores in halite fluid inclusions and on Mars, *Radiat. Res.*, *159*, 722–729, doi:10.1667/0033-7587(2003)159[0722:RLFTVO]2.0.CO;2.

Lachenbruch, A. (1962), Mechanics of thermal contraction cracks and ice-wedge polygons in permafrost, *Spec. Pap. Geol. Soc. Am.*, *70*, 69 pp.

Laskar, J., A. C. M. Correia, M. Gastineau, F. Joutela, B. Levrarda, and P. Robutela (2004), Long term evolution and chaotic diffusion of the insolation quantities of Mars, *Icarus*, *170*, 343–364, doi:10.1016/j.icarus.2004.04.005.

Lebron, I., D. A. Robinson, S. Goldberg, and S. M. Lesch (2004), The dielectric permittivity of calcite and arid zone soils with carbonate minerals, *Soil Sci. Soc. Am. J.*, *68*, 1549–1559.

Leighton, R. B., and B. Murray (1966), Behavior of carbon dioxide and other volatiles on Mars, *Science*, *153*, 136–144, doi:10.1126/science.153.3732.136.

McEwen, A. S., et al. (2007), A closer look at water-related geologic activity on Mars, *Science*, *317*, 1706–1709, doi:10.1126/science.1143987.

Mellon, M. T. (1997), Small-scale polygonal features on Mars: Seasonal thermal contraction cracks in permafrost, *J. Geophys. Res.*, *102*, 25,617–25,628, doi:10.1029/97JE02582.

Mellon, M. T., B. M. Jakosky, H. H. Kieffer, and P. R. Christensen (2000), High-resolution thermal inertia mapping from the Mars Global Surveyor Thermal Emission Spectrometer, *Icarus*, *148*, 437–455, doi:10.1006/icar.2000.6503.

Mischna, M. A., M. I. Richardson, R. J. Wilson, and D. J. McCleese (2003), On the orbital forcing of Martian water and CO_2 cycles: A general circulation model study with simplified volatile schemes, *J. Geophys. Res.*, *108*(E6), 5062, doi:10.1029/2003JE002051.

Napijalo, M. Lj., Z. Nikoliæ, J. Dojèiloviæ, M. M. Napijalo, and L. Novakoviæ (1998), Temperature dependence of electric permittivity of linear dielectrics with ionic and polar covalent bonds, *J. Phys. Chem. Solids*, *59*, 1255–1258.

Olhoeft, G. R. (1978), Electrical properties of permafrost, in *Proceedings of the Third International Conference on Permafrost*, pp. 127–131, Natl. Res. Counc. of Can., Ottawa, Ontario.

Olhoeft, G. R. (1981), Electrical properties of rocks, in *Physical Properties of Rocks and Minerals*, edited by Y. S. Touloukian et al., pp. 257–330, McGraw-Hill, New York.

Pollack, J. B., and O. B. Toon (1982), Quasi-periodic climate change on Mars: A review, *Icarus*, *50*, 259–287, doi:10.1016/0019-1035(82)90126-9.

Pozdnyakov, A. I., and K. Y. Chan (1979), The technique of the electrical sounding and profiling in soil investigations (in Russian), *Vestn. Mosk. Univ.*, *1*, 46–54.

Price, B. P., and T. Sowers (2004), Temperature dependence of metabolic rates for microbial growth, maintenance, and survival, *Proc. Natl. Acad. Sci. U. S. A.*, *101*, 4631–4636, doi:10.1073/pnas.0400522101.

Rivkina, E. M., E. I. Friedmann, C. P. McKay, and D. A. Gilchinsky (2000), Metabolic activity of permafrost bacteria below the freezing point, *Appl. Environ. Microbiol.*, *66*, 3230–3233, doi:10.1128/AEM.66.8.3230-3233.2000.

Rossbacher, L. A., and S. Judson (1981), Ground ice on Mars: Inventory, distribution, and resulting land forms, *Icarus*, *45*, 39–59, doi:10.1016/0019-1035(81)90005-1.

Schorghofer, N., and O. Aharonson (2005), Stability and exchange of subsurface ice on Mars, *J. Geophys. Res.*, *110*, E05003, doi:10.1029/2004JE002350.

Smith, P. H., et al. (2008), Introduction to special section on the Phoenix Mission: Landing Site Characterization Experiments, Mission Overviews, and Expected Science, *J. Geophys. Res.*, *113*, E00A18, doi:10.1029/2008JE003083.

Squyres, S. (1986), Geomorphic evidence for the distribution of ground ice on Mars, *Science*, *231*, 249–252, doi:10.1126/science.231.4735.249.

Sweeney, J. J., J. J. Roberts, and P. E. Harben (2007), Study of dielectric properties of dry and saturated Green River oil shale, *Energy Fuels*, *21*, 2769–2777, doi:10.1021/ef070150w.

Toon, O. B., J. B. Pollack, W. Ward, J. A. Burns, and K. Bilski (1980), The astronomical theory of climatic change on Mars, *Icarus*, *44*, 552–607, doi:10.1016/0019-1035(80)90130-X.

Topp, G. C., J. L. Davis, and A. P. Annan (1980), Electromagnetic determination of soil water content: Measurements in coaxial transmission lines, *Water Resour. Res.*, *16*, 574–582, doi:10.1029/WR016i003p00574.

Tschimmel, M., N. I. Ignatiev, D. V. Titov, E. Lellouch, T. Fouchet, M. Giuranna, and V. Formisano (2008), Investigation of water vapor on Mars with PFS/SW of Mars Express, *Icarus*, *195*, 557–575.

Zent, A. P. (2008), An historical search for thin H_2O films at the Phoenix landing site, *Icarus*, *196*, 385–408, doi:10.1016/j.icarus.2007.12.028.

C. S. Campbell, G. S. Campbell, and D. R. Cobos, Decagon Devices, 2345 NE Hopkins Court, Pullman, WA 99163, USA.

G. Cardell, M. C. Foote, and M. H. Hecht, Jet Propulsion Laboratory, 4800 Oak Grove Drive, Pasadena, CA 91109, USA.

M. Mehta, Department of Atmospheric, Oceanic and Space Sciences, University of Michigan, Ann Arbor, MI 48109, USA.

S. E. Wood, University of Washington, 367 Johnson Hall, Seattle, WA 98195, USA.

A. P. Zent, Planetary Systems Branch, NASA Ames Research Center, MS 245-3, Moffett Field, CA 94035, USA. (Aaron.P.Zent@nasa.gov)